International Reviews, Research and Studies in the Field of Materials and Metallurgy Engineering

EDITOR
PROF. DR. KİNYAS POLAT

SERÜVEN YAYINEVİ

Genel Yayın Yönetmeni / Editor in Chief • C. Cansın Selin Temana

Kapak & İç Tasarım / Cover & Interior Design • Serüven Yayınevi

Birinci Basım / First Edition • © Aralık 2025

ISBN • 978-625-8682-82-3

Serüven Yayınevi / Serüven Publishing
Türkiye Adres / Turkey Address: Kızılay Mah. Fevzi Çakmak 1. Sokak
Ümit Apt No: 22/A Çankaya/ANKARA
Telefon / Phone: 05437675765
web: www.seruvenyayinevi.com
e-mail: seruvenyayinevi@gmail.com

Baskı & Cilt / Printing & Volume
Sertifika / Certificate No: 47083

INTERNATIONAL REVIEWS, RESEARCH AND STUDIES IN THE FIELD OF MATERIALS AND METALLURGY ENGINEERING

EDITOR

PROF. DR. KİNYAS POLAT

Contents

Chapter 1

INVESTIGATION OF THE FACTORS CAUSING MECHANICAL IRREGULARITIES AT FEB/ FE2B INTERFACE

İzzet Paruğ DURU[1], Polat TOPUZ[2], Tuna AYDOĞMUŞ[3]

1 Assoc. Prof. Dr. İstanbul Gedik University, Gedik Vocational School, İstanbul, Türkiye, parug.duru@gedik.edu.tr ORCID ID:
2 Assoc. Prof. Dr. İstanbul Gedik University, Gedik Vocational School, İstanbul, Türkiye, polat.topuz@gedik.edu.tr ORCID ID:
3 Assoc. Prof. Dr. Hitit University, Hitit Technical Sciences Vocational School, Çorum, Türkiye, tunaaydogmus@hotmail.com ORCID ID: 0000-0002-8736-2949

1. Introduction

Nowadays, various processes can be carried out to improve the surface properties of materials. As a result of these processes, the surface properties of the materials are improved while their internal structures maintain their original properties (Mozetič, 2019). Coating methods, hardening methods or diffusion controlled processes can be applied to improve the surface properties of materials. Generally, the layers formed on the surfaces of the materials as a result of these processes are harder or softer, wear resistant, corrosion resistant, chemical resistant and have similar properties, depending on the original material structure. These properties that can be imparted to the surface of the material vary depending on the surface treatment applied (Davis, 2002).

Boronizing, which is a diffusion-controlled process, is one of the methods that improves the surface properties of materials, especially in terms of hardness, wear resistance and partial corrosion resistance. Although it is mostly applied to metallic materials, it can also be applied to non-ferrous and cermet materials. The boronizing process is a method that can be carried out in solid, liquid, gas and plasma environments, and can be carried out using different boronizing components (Colás & Totten, 2016).

Pack-boronizing, which is one of the boronizing methods in solid media, stands out as one of the most widely used methods. In principle, it is the heat treatment of the material covered with boronizing agent in a heat treatment crucible at appropriate temperatures and time (Gissler & Jehn, 1992). Schematical pack-boronizing treatment shown in Fig.1.

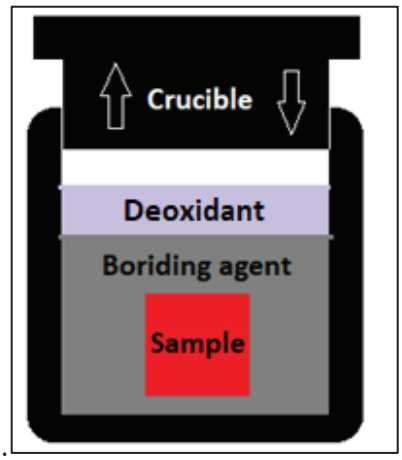

Figure 1. Schematical pack-boronizing treatment

As a result of the process, boride layers are formed on the surface of the materials, which form compounds with some of the elements in their composition. For example, boronizing of the steel materials, mostly double phase (FeB+Fe_2B) or single phase (Fe_2B) boride layers are formed on their

surfaces (Sinha, 1991). In particular, the morphology and thickness of these layers vary with the alloy elements found in the structure of the boronized steel as well as the applied heat treatment. If we need to explain the effects of alloying elements in steel on boronizing in more detail; For example, "Cr" affects both the morphology and thickness of the boride layer. As the amount of chromium contained in the steel increases, the properties of the boride layer develop positively, while the layer thickness decreases, it also becomes planar. The "Ni" element reduces the boride layer thickness, and as its amount increases, it turns the morphology of the layer into a columnar, namely sawtooth appearance. Similarly, the “Mn” and “V” elements both reduce the layer thickness and turn the morphology into columnar (Lin & Cheng, 1987; Rus, 1985; Sahin & Meric, 2002; Sinha, 1991). The changes in the iron boride layer depending on the type and amount of alloying elements in the steel are given in the examples in Fig.2.

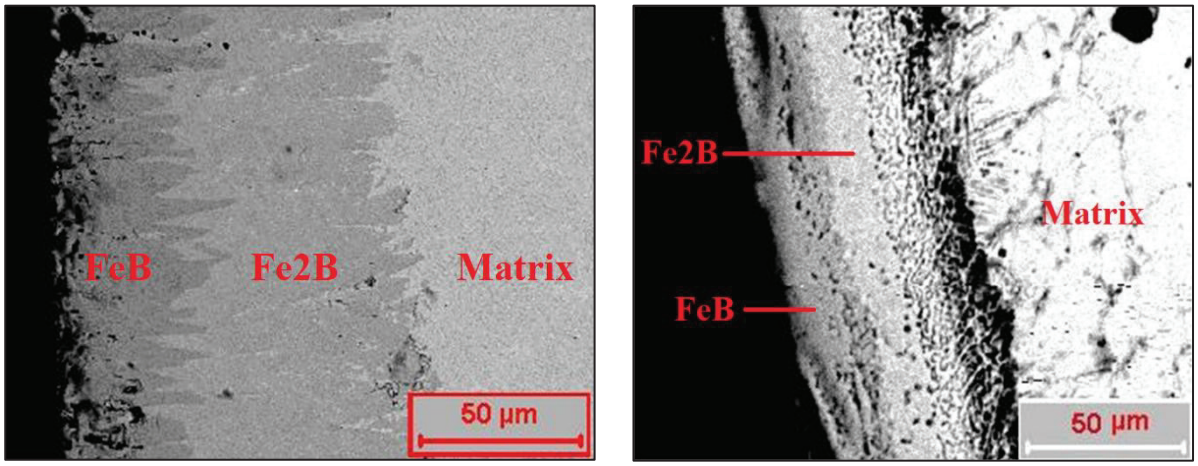

(a) (b)

Figure 2. Formation of a dual phase iron boride (FeB+Fe_2B) layer on the surface of different steels a) Low alloy medium carbon steel. b) Austenitic stainless steel (Topuz, 2009).

Fig.2 (a) emphasizes the dual-phase iron boride layer formed on the surface of low alloy steel has a columnar (saw tooth-like) structure, while the dual-phase iron boride layer formed on the surface of stainless steel with high chromium and nickel content has a planar structure. Although iron borides consisting mainly of FeB and Fe_2B phases are formed on the surfaces of steels by boronizing, the alloying elements in them also interact with boron and form boride phases compatible with themselves. Examples of these are chromium-borides, nickel-borides, titanium-borides, tungsten-borides, molybdenum-borides, etc (Gogotsi & Andrievski, 2012). However, since the other borides formed apart from iron borides are in very low amounts, they can be detected by XRD analysis.

The dual-phase layer formed on the steel surface also has some disadvantages. As a result of the differences in the properties of the FeB and Fe_2B phases, cracking, separation or breakage between the phases can be observed. This becomes more likely as the layer thickens. One of the most

fundamental factors that create this situation is that the thermal expansion coefficients of these phases are different from each other. Due to this factor, the phases are forced to separate because they apply a push-pull motion to each other. Other factors that cause layer separation are the differences in hardness and elasticity modules of these phases. Due to these negative situations, it is desired to form a single-phase layer consisting of only Fe_2B on the steel surface as a result of boronizing (Sinha, 1991). An example microstructure showing the separation of FeB and Fe_2B phases as a result of the boronizing process in some steels is given in Fig.3.

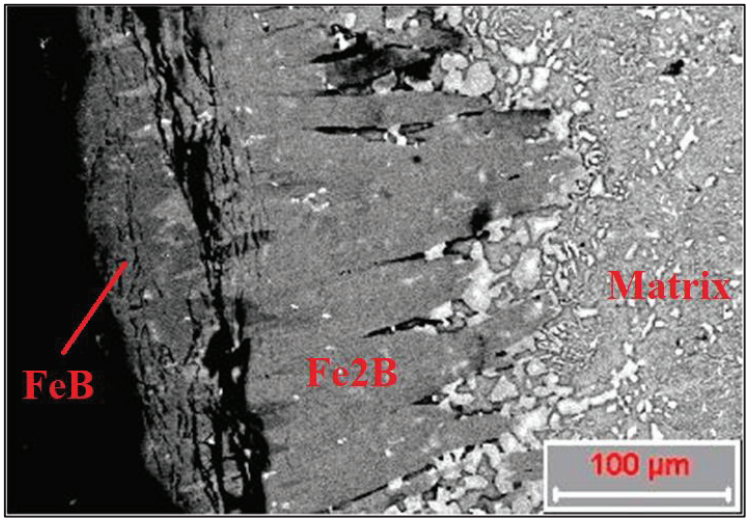

Figure 3. Interphase seperation in boronized 60WCrV7 steel [9]

As can be seen from the figure, as a result of boronization of 60WCrV7 steel, separation occurred between the FeB phase and the Fe_2B phase in the dual-phase iron boride layer formed on the surface.

The mechanical and chemical characteristics of borided steels are influenced by the thickness of the created layer, referred to as the case depth, which relies on the boriding temperature, duration of treatment, and the boron concentration in proximity to the sample surface (Campos-Silva et al., 2012). As the duration of treatment and temperature increase, the FeB regions significantly thicken, evolving from compact, aligned Fe_2B crystals. These phases predominantly tend to expand along the (002) plane, resulting in heightened mechanical stress at the FeB/Fe_2B interface because of the considerable difference in their thermal expansion coefficients within the temperature range of 473 to 873 K (Rile, 1974). Gao et al. focus on interfacial bonding to reveal the most stable configuration of Al4C3 and Al layers using DFT. The interface is primarily maintained by metallic Al-Al interactions and covalent Al-C interactions. The C-terminated interface shows stronger bonding compared to the Al-terminated interface. Nonetheless, when an excess of dangling bonds exists at the C-terminated interface, considerable electron transfer occurs in the surface Al atoms. This diminishes the Al-Al metallic bonding in both the

surface and subsurface layers of the Al slab, ultimately resulting in a breakdown within the aluminum matrix (Gao et al., 2025).

In this study, the separation/cracking occur at FeB/Fe_2B interface is considered. Density functional theory (DFT) is preferred to handle the problem in atomistic manner. The computational procedure is detailed in Section 2. The results are elaborately given and discussed in latter section. In Section 4, the content is concluded summarizing the striking findings.

2. Computational Method

This work focus on FeB/Fe_2B interface formed through boriding steel. The composition of steel is not literally considered in theoretical calculations. Note that precalculations which handles Fe_2B body centered tetragonal and FeB orthorhombic result in a remarkable lattice mismatch and instability. We assume that FeB/Fe_2B interface atoms obey to tetragonal system. It is due to prevent the lattice mismatch that sabotage the growth of FeB layer on Fe_2B. Hence, the crsytal parameters of FeB used in DFT calculations is not consistent to experimental data. The mechanical calculations literally fail when the interface is composed of single unit cells. The unit cell is repeated through c-axis by 4 times. A vacuum slab is set to prevent the atomic interactions between Fe_2B and FeB structures. even it is adequately optimized. FeB and Fe_2B, which are the basic boride phases formed on the surfaces of steels by boronizing, are given in Table 1.

Table 1. Structural, mechanical, thermal, and electrical properties of FeB and Fe_2B

Specifications	**Iron Boride Type**	
	Fe_2B	**FeB**
Crystal structure	Body centered tetragonal	Orthorhombic
Boron content (wt.%)	8.83	16.23
Lattice parameter (Å)	a=5.185, c=4.136	a=4.062, b=5.505, c=2.947 (Kumar et al., 2017)
Theoretical density ($g.cm^{-3}$)	7.43	6.75
Melting degree (C)	1389 - 1410	1540 - 1657
Thermal conductivity ($W.mK^{-1}$)	30.1 (in room temp.)	10.0 (in room temp.)
Thermal expansion coefficient ($ppm.C^{-1}$)	6.9 (20 – 300 C)	9.3 (20 – 300 C) (Lyakhovich, 1975)

Elastic modulus (GPa)	290	590
Micro-hardness (GPa)	18 - 20	19 - 21
Electrical resistance (10^{-9} Ω.cm.K^{-2})	3.08	2.94
Curie temperature (℃)	742	325

The first-principles calculations are conducted using Cambridge Serial Total Energy Package (CASTEP) code (Clark et al., 2005), which operates based on density functional theory (DFT) within a plane-wave pseudopotential. Kohn-Sham equations (Hohenberg & Kohn, 1964; Kohn & Sham, 1965) are solved utilizing LDA-CA-PZ for the exchange-correlation energy. A geometry optimization takes place before ground state energy and elastic properties calculations in GGA-PBE (Perdew, Burke, & Ernzerhof, 1996) scheme. Vanderbilt-type ultrasoft pseudopotentials are employed to accurately include electron-ion interactions (Vanderbilt, 1990). We set a plane-wave cutoff energy of 354 eV. The crystal structures underwent full relaxation using the Broyden-Fletcher-Goldfarb-Shanno (BFGS) minimization technique. K-point is set to gamma. The elastic properties are revealed using finite strain theory, deriving the elastic constants as proportionality coefficients that relate the applied strain to the computed stress, represented by the equation $\sigma_i = C_{ij}\varepsilon j$. In addition, the authors evaluate the polycrystalline bulk modulus (B) and shear modulus (G) by the Voigt-Reuss-Hill approximation.

3. Results & Discussion

The elastic stiffness constants (C_{ij}) characterize a material's resistance to deformation under stress, while the compliance constants (S_{ij}) reflect its ability to deform when subjected to mechanical forces. Higher stiffness constants indicate stronger bonding forces and enhanced structural stability, whereas higher compliance values signify increased flexibility. C_{ij} and Sij are given in Eq.1 and Eq.2, respectively.

$$C_{ij} = \begin{pmatrix} 405.81095 & 303.10505 & -85.20705 & 0 & 0 & 0 \\ 303.10505 & 124.98170 & 237.53333 & 0 & 0 & 0 \\ -85.20705 & 237.53333 & -320.53715 & 0 & 0 & 0 \\ 0 & 0 & 0 & 89.84455 & 0 & 0 \\ 0 & 0 & 0 & 0 & 194.24625 & 0 \\ 0 & 0 & 0 & 0 & 0 & 141.04125 \end{pmatrix} \quad (1)$$

$$S_{ij} = \begin{pmatrix} 0.0042165 & -0.0033614 & -0.0036118 & 0 & 0 & 0 \\ -0.0033614 & 0.0060019 & 0.0053413 & 0 & 0 & 0 \\ -0.0036118 & 0.0053413 & 0.0017985 & 0 & 0 & 0 \\ 0 & 0 & 0 & 0.0111303 & 0 & 0 \\ 0 & 0 & 0 & 0 & 0.0051481 & 0 \\ 0 & 0 & 0 & 0 & 0 & 0.0070901 \end{pmatrix} \quad (2)$$

Born stability criteria (Born, 1940) helps to demonstrate the mechanical stability. The following inequalities (Eq.3) (Petukhov, 2022) are applied to elastic stiffness matrix for a tetragonal system.

$$c_{11} > |c_{12}|,\ c_{44} > 0,\ c_{66} > 0,\ (c_{11} + c_{12})c_{33} > 2(c_{13})^2 \quad (3)$$

According to below, FeB/Fe_2B is instable, most probably, due to the interfacial interactions. Each surfaces occasionally cause a spatial displacement through opposite directions, moreover form mechanical cracks.

Materials have unique coefficients of thermal expansion. During heating or cooling, one crystal may expand or contract more than its counterpart, resulting in internal stresses at the interface. Continuous thermal cycling can lead to stress accumulation, ultimately causing cracks. However, the atomic bonds formed at an interface are often weaker than those within each individual crystal. In layered magnetic structures, imperfect bonding at the interface can lead to crack initiation under applied stress. The interface serves as a natural site for the accumulation of dislocations or point defects during crystal growth and deformation. These defects tend to concentrate stress, diminishing local mechanical strength and enhancing the likelihood of crack nucleation. In particular, grain boundaries within polycrystalline materials often act as stress concentrators where cracks can initiate under mechanical load. In this paper defects are not considered. When one crystal undergoes a phase transformation—such as a change in crystal structure or magnetic phase—while an adjacent crystal remains unchanged, significant stress can develop at the interface. These stresses may exceed the material's fracture toughness, leading to crack formation. For instance, martensitic phase transformations in steel can cause cracks to form at grain boundaries or phase interfaces. The cracks may be originated from incomplete Diffusion or Solid-State Reactions. During the processes of crystal growth or material synthesis, incomplete diffusion at the interface can result in residual stresses and localized weak points. Such inconsistencies are often the precursors to microcrack initiation. For example, in Fe-B materials, inadequate diffusion during fabrication can induce stress gradients that trigger crack formation. Table 2 includes Young modulus and Poisson ratios which are directly derived from C_{ij}.

Table 2. Young modulus and Poisson ratios of FeB/Fe_2B interface (GPa)

Axis	Young Modulus (GPa)	Poisson Ratios			
X	237.16208	$\mathbf{E_{xy}}$	0.7972	$\mathbf{E_{xz}}$	0.8566
Y	166.61259	$\mathbf{E_{yx}}$	0.5601	$\mathbf{E_{yz}}$	-0.8899
Z	556.01752	$\mathbf{E_{zx}}$	2.0082	$\mathbf{E_{zy}}$	-2.9698

The Young's modulus of 237.16 GPa reveals significant stiffness along the x-axis, suggesting a robust mechanical framework. The Poisson ratios E_{xy} = 0.7972 and E_{xz} = 0.8566 imply that considerable lateral strain occurs when the material is compressed or stretched along the x-axis. These relatively high Poisson ratios suggest substantial dimensional changes in the perpendicular directions as a result of mechanical deformation along the x-axis. Along the y-axis, the Young's modulus of 166.61 GPa indicates moderate stiffness. The Poisson ratios E_{yx}= 0.5601 and E_{yz} = -0.8899 demonstrate anisotropic behavior. Notably, the negative value of E_{yz} points to auxetic behavior in this direction, where the material expands laterally when stretched. Young's modulus of 556.02 GPa along the z-axis signifies extreme stiffness and exceptional mechanical stability. The Poisson ratios E_{zx} = 2.0082 and E_{zy}= -2.9698 reveal unconventional deformation behavior. The large positive Poisson ratio (E_{zx}) suggests significant lateral expansion under compression, while the highly negative Poisson ratio (E_{zy}) indicates considerable shrinkage when stretched along the z-axis. This pronounced anisotropy underscores the directional dependence of the material's mechanical response.

Table 3 displays elastic constants of polycrystalline FeB/Fe_2B interface considering Voigt, Reus, and Hill representations. According to Voigt-Reuss-Hill approximation (Hill, 1952), G_H and B_H are obtained from Eq.4.

$$G_H = \frac{1}{2}(G_R + G_V) \qquad B_H = \frac{1}{2}(B_R + B_V) \tag{4}$$

Table 3. Elastic constants of polycrystalline FeB/Fe_2B interface (GPa)

	Voigt	**Reuss**	**Hill**
Bulk Modulus	124.56868	114.24653	119.40761
Shear Modulus (Lame Mu)	68.68135	120.28719	94.48427
Lame Lambda	78.78111	34.05507	56.41809
Young Modulus	174.05539	267.11532	224.29352
Poisson Ratio	0.26712	0.11032	0.18694
Hardness (Tian 2012)	9.33847	28.97511	17.64984

The bulk modulus values range from 114.25 GPa (Reuss) to 124.57 GPa (Voigt), indicating moderate resistance to uniform compression and aligning with the material's strong structural characteristics. In contrast, the shear modulus values show considerable variability, spanning from 68.68 GPa (Voigt) to 120.29 GPa (Reuss), which reflects significant anisotropy in the material’s resistance to shear

deformation. The differences between these values illustrate that the shear response can vary dramatically across different orientations. The calculated Young's modulus ranges from 174.06 GPa (Voigt) to 267.12 GPa (Reuss), with an average of 224.29 GPa (Hill). This range highlights the material's complex mechanical behavior, indicating that certain crystal orientations provide much greater stiffness than others. Poisson ratio values, which fall between 0.110 and 0.267, demonstrate variability in lateral deformation under different loading conditions. Generally, lower Poisson ratios tend to indicate improved shear resistance, while higher ratios correspond to more significant dimensional changes under stress.

Hardness is defined as the resistance of a material to deformation and may be predicted using macroscopic and microscopic models. In this work, we use the semi-empirical equations of hardness proposed by Tian et al. (Tian, Xu, & Zhao, 2012) (Eq.5).

$$H_V = 0.92k^{1.137}G^{0.708} \tag{5}$$

where k = G/B, G and B are the shear modulus and the bulk, respectively. Hardness values range from 9.34 to 28.98 GPa, suggesting that the FeB/Fe_2B interface exhibits both moderate and notably high hardness levels, influenced by mechanical stress orientation and microstructural characteristics. The anisotropic mechanical properties of the compounds are very important in applications. Based on the G and B values from Reuss and Voigt, Ranganathan et al. (Ranganathan & Ostoja-Starzewski, 2008) proposed a universal elastic anisotropy index A_U for crystal with any symmetry as shown below:

$$A_U = \frac{5G_V}{G_R} + \frac{B_V}{V_R} - 6 \tag{6}$$

A_U, -2.05476, emphasizes the pronounced anisotropic nature of this interface, consistent with the observed mechanical variability. However, a high Debye temperature generally correlates with strong bonding and good thermal conductivity. The evaluation of the elastic Debye temperature is conducted using Anderson's methodology (Born, 1940), and it is proportional to the averaged sound velocity which is given in Eq.7.

$$\theta = \frac{h}{k_B}\left[\frac{3q}{4\pi}\frac{N\rho}{M}\right]^{1/3} \upsilon_m \tag{7}$$

N denotes Avogadro's number while ρ and M are density and molecular weight of the solid, respectively. Besides, q represents the number of atoms in the molecule where h is the Planck

constant, and k is the Boltzmann constant. From Hill perspective, Debye temperature is almost equal to 720 K.

$$\upsilon_m = \left[\frac{1}{3}\left(\frac{2}{\upsilon_t{}^3} + \frac{1}{\upsilon_l{}^3}\right)\right]^{-1/3} \tag{8}$$

υ_m can be determined by transverse sound velocity, $\upsilon_t = \left(\frac{3B+4G}{3\rho}\right)^{1/2}$, and longitudinal sound velocity, $\upsilon_l = \left(\frac{G}{\rho}\right)^{1/2}$. Additionally, the melting point is calculated using $T_m \approx 354 + 4.5 \times B$ (Xiao, Yang, Pi, & Zhang, 2022) which is accurately viable for tetragonal systems. Sound velocity, Debye temperature and melting points can be tracked from Table 4.

Table 4. Sound velocity, Debye temperature and melting point of FeB/Fe_2B interface

	Voigt	**Reuss**	**Hill**
vl(m/s)	3835,930956	5076,461067	4499,156769
vt(m/s)	6804,916095	7670,522066	7250,648039
vm(m/s)	4995,577486	6286,452589	5696,760363
TD (K)	631,12	794,21	719,71
Tm (K)	914,56	868,11	891,33

The longitudinal sound velocity ranges from 3835 m/s to 5076 m/s, while the transverse velocity varies between 6804 m/s and 7670 m/s. The mean sound velocity, calculated to be between 4995 m/s and 6286 m/s, reflects the material's capability to transmit mechanical waves effectively. Generally, higher sound velocities correspond to greater stiffness and stronger atomic bonding. The Debye temperature extends from 631 K to 794 K, indicating robust lattice vibrations and strong interatomic bonding. Materials with elevated Debye temperatures typically show enhanced thermal conductivity and mechanical resilience. The melting point varies between 868 K and 914 K, confirming the material's high thermal stability, which is essential for applications requiring resistance to elevated temperatures and mechanical stress. In our case, while bulk FeB and Fe_2B may exhibit high melting points, their interface behaves like a high-energy phase with reduced stability.

Table 5. Thermodynamics and mechanical behavior of FeB and Fe_2B.

	Method	Crystal space	Debye Temp. (K)	Young's Modulus (GPa)	Bulk Modulus (GPa)	Shear Modulus (GPa)	T_m (K)	Ref.
FeB	spark plasma sintering	Orthorhombic	659.5± 0.1	267±1	174± 1	107.4± 0.1	1931	(Haynes, 2016)
Fe_2B	Pulse echo technique	Tetragonal	620	252	182	107	1662	(Haynes, 2016; Nakamori et al., 2016)
Fe_2B	DFT	Tetragonal	685	355.2	222.3	144.0	2165	(Li, Wang, Hu, & Wei, 2014)
FeB/Fe_2B interface	DFT	Tetragonal	719.71	224.29	119.41	94.48	891.33	This work

Table 5 underlines that FeB and Fe_2B are individually show high melting temperatures in contrast to FeB/Fe_2B interface. The system aims to minimize interfacial energy during processes such as melting or phase transitions. This reduction in energy facilitates atomic diffusion, which is particularly pronounced at lower temperatures in areas with high interfacial energy. However, the interface functions as a unique phase boundary that possesses lower thermodynamic stability, especially in systems where multiple phases coexist. Moreover, interfacial regions are typically energetically less favorable and they inherently exhibit reduced thermal stability. In crystalline materials, the boundary between two phases creates a discontinuity in the arrangement of atoms. As a result, atoms at the

interface often find themselves in a less favorable coordination environment compared to those located in the bulk material. The auxetic behavior in the interface may provide a repulsion to lead instability.

4. Conclusion

Boronizing process causes growth of an iron boride layer consisting mostly of FeB + Fe_2B phases on the surface of the steels. Iron boride formations in different steels and possible separations between phases are extensiveley encountered. This study has shown that this separation between phases is related not only by differences in thermal expansion coefficients of layers but also mechanical repulsion applied by the interface atoms. DFT theory is used to figure out mechanical behavior. Born criteria is applied to elastic stiffness constants check the stability of the interface. The considered structure is found to be instable. Negative Poisson ratios support the auxetic behavior between y and z directions. This may disclose instabilities and cracks at interface. However, melting temperature is quite low. It can mediate a slippery surface decreasing the adherence beween layers. Especially when focusing on the interface of phases, different values of the fundamental properties of FeB and Fe_2B have emerged. Considering that the separations between phases occur at these interfaces, subsequent studies should be considered in this direction.

References

Born, M. (1940). *On the stability of crystal lattices. I.* Paper presented at the Mathematical

Proceedings of the Cambridge Philosophical Society.

Campos-Silva, I., Ortiz-Domínguez, M., Tapia-Quintero, C., Rodriguez-Castro, G., Jiménez-Reyes, M., & Chávez-Gutiérrez, E. (2012). Kinetics and boron diffusion in the FeB/Fe2B layers formed at the surface of borided high-alloy steel. *Journal of Materials Engineering and Performance, 21*(8), 1714-1723.

Clark, S. J., Segall, M. D., Pickard, C. J., Hasnip, P. J., Probert, M. I., Refson, K., & Payne, M. C. (2005). First principles methods using CASTEP. *Zeitschrift für kristallographie-crystalline materials, 220*(5-6), 567-570.

Colás, R., & Totten, G. E. (2016). *Encyclopedia of iron, steel, and their alloys (Online version)*: CRC Press.

Davis, J. R. (2002). *Surface hardening of steels: understanding the basics*: ASM international.

Gao, N., Zhong, Z., Liu, L., Lu, X., Fan, T., & Zhou, X. (2025). First-principles study on the interfacial stability, mechanical behavior and failure mechanism of Al4C3 (0 0 0 1)/Al (1 1 1) interfaces. *Surfaces and Interfaces, 62*, 106277.

Gissler, W., & Jehn, H. A. (1992). *Advanced techniques for surface engineering* (Vol. 14658): Springer Science & Business Media.

Gogotsi, Y. G., & Andrievski, R. A. (2012). *Materials science of carbides, nitrides and borides* (Vol. 68): Springer Science & Business Media.

Haynes, W. M. (2016). *CRC handbook of chemistry and physics*: CRC press.

Hill, R. (1952). The elastic behaviour of a crystalline aggregate. *Proceedings of the Physical Society. Section A, 65*(5), 349.

Hohenberg, P., & Kohn, W. (1964). Inhomogeneous electron gas. *Physical review, 136*(3B), B864.

Kohn, W., & Sham, L. J. (1965). Self-consistent equations including exchange and correlation effects. *Physical review, 140*(4A), A1133.

Kumar, P. A., Satya, A., Reddy, P. S., Sekar, M., Kanchana, V., Vaitheeswaran, G., . . . Shekar, N. C. (2017). Structural and low temperature transport properties of Fe2B and FeB systems at high pressure. *Journal of Physics and Chemistry of Solids, 109*, 18-25.

Li, L.-H., Wang, W.-L., Hu, L., & Wei, B.-B. (2014). First-principle calculations of structural, elastic and thermodynamic properties of Fe–B compounds. *Intermetallics, 46*, 211-221.

Lin, H.-R., & Cheng, G.-H. (1987). Hardenability effect of boron on carbon steels. *Materials Science and Technology, 3*(10), 855-859.

Lyakhovich, L. S., Kosachevskii, L.N, Kulik, A.Y, Surkov V.V, Turov Y.V. (1975). Soviet materials science: a transl. of Fiziko-khimicheskaya mekhanika materialov *Academy of Sciences of the Ukrainian SSR, 9*, 272-275.

Mozetič, M. (2019). Surface modification to improve properties of materials. *Materials, 12*(3), 441.

Nakamori, F., Ohishi, Y., Kumagai, M., Muta, H., Kurosaki, K., Yamanaka, S., & Fukumoto, K.-i. (2016). Mechanical and thermal properties of Fe2B.

Perdew, J. P., Burke, K., & Ernzerhof, M. (1996). Generalized gradient approximation made simple. *Physical review letters, 77*(18), 3865.

Petukhov, B. (2022). Transition from solid-solution softening to hardening in the plasticity of crystalline materials as a manifestation of quasi-localization of dislocation kinks. *Phys. Sol. State, 64*(12), 1939-1945.

Ranganathan, S. I., & Ostoja-Starzewski, M. (2008). Universal elastic anisotropy index. *Physical review letters, 101*(5), 055504.

Rile, M. (1974). Reasons for the formation of cracks in boride coatings on steel. *Metal Science and Heat Treatment, 16*(10), 836-838.

Rus, J., De Leal, C.L. and Tsipas, D.N. . (1985). Boronizing of 304 Steel. *Journal of materials science letters, 4*, 558-560.

Sahin, S., & Meric, C. (2002). Investigation of the effect of boronizing on cast irons. *Materials Research Bulletin, 37*(5), 971-979.

Sinha, A. (1991). *Heat treatment* (Vol. 4).

Tian, Y., Xu, B., & Zhao, Z. (2012). Microscopic theory of hardness and design of novel superhard crystals. *International Journal of Refractory Metals and Hard Materials, 33*, 93-106.

Topuz, P. (2009). *Development of boronizing parameters and boronizing of different steels in fluidized bed furnace.* Marmara University, Istanbul.

Vanderbilt, D. (1990). Soft self-consistent pseudopotentials in a generalized eigenvalue formalism. *Physical Review B, 41*(11), 7892.

Xiao, W., Yang, Y., Pi, Z., & Zhang, F. (2022). Phase stability and mechanical properties of the monoclinic, monoclinic-prime and tetragonal REMO4 (M= Ta, Nb) from first-principles calculations. *Coatings, 12*(1), 73.

Chapter 2

GAS-ASSISTED POWDER INJECTION MOLDING: PROCESS FUNDAMENTALS, MICROSTRUCTURAL EVOLUTION, AND FUNCTIONAL PERFORMANCE

Bünyamin ÇİÇEK[1], Yavuz SUN[2]

1 Hitit University, Technical Sciences Vocational School, Çorum, Türkiye
ORDID: https://orcid.org/0000-0002-6603-7178
2 Karabuk University, Engineering and Natural Sciences Faculty, Karabük, Türkiye
ORCID: https://orcid.org/0000-0002-7336-5591

1. Introduction

Powder Injection Molding (PIM) has emerged as a mature manufacturing route that combines the geometric freedom of polymer injection molding with the material versatility of powder metallurgy. Since its systematic formulation in the 1980s, PIM has enabled the production of complex-shaped metallic components with high dimensional accuracy and near-net-shape capability, particularly for stainless steels and advanced alloys (German, 1984, 1990). The method relies on the preparation of a homogeneous feedstock composed of fine metal powders and multicomponent polymer binders, followed by molding, debinding, and sintering stages. Despite its industrial success, conventional PIM systems remain highly sensitive to feedstock homogeneity, powder–binder interactions, and process-induced defects, which directly influence final microstructure and performance (German, Hens, & Lin, 1991; Hartwig et al., 1998).

Binder system design has been recognized as one of the most critical parameters governing the success of PIM processing. In particular, PEG–PMMA-based binder systems have attracted significant attention due to their favorable rheological behavior, solvent debinding capability, and structural stability during molding (Bakan, Jumadi, Messer, Davies, & Ellis, 1998; Omar, Davies, Messer, & Ellis, 2001). Numerous studies have demonstrated that appropriate control of binder composition and powder loading can significantly improve green part integrity and reduce defect formation during debinding (Li, Huang, Qu, & Li, 1999; Yang, Yang, Wang, & Hon, 2003). However, even with optimized feedstock formulations, conventional screw- or hydraulically driven injection systems often introduce shear-induced segregation, non-uniform flow fronts, and localized binder depletion, especially when processing fine powders or reactive alloys (Anderson, Groza, Fendorf, & Echer, 1999; Rak, 1998).

These limitations become more pronounced when PIM is extended to reactive metals and biomaterial systems such as magnesium alloys or biomedical-grade stainless steels. Magnesium-based materials, while attractive for lightweight and biodegradable applications, exhibit high oxidation affinity and narrow processing windows during sintering (Friedrich & Schumann, 2001; Wolff, Ebel, & Dahms, 2010). Similarly, biomedical alloys such as 316L stainless steel demand strict control over residual oxides, porosity, and microstructural continuity to ensure corrosion resistance and biocompatibility (Zheng, Gu, Xi, & Chai, 2010). As a result, the injection stage itself—often treated as a purely mechanical transfer process—plays a decisive role in determining the success of downstream sintering and functional performance.

In response to these challenges, alternative injection strategies have been proposed to decouple feedstock transport from excessive mechanical shear and pressure gradients. Among these, gas-assisted injection concepts represent a promising but still underexplored approach within the PIM field. By utilizing inert gas pressure to drive the flow of a gel-phase feedstock, such systems aim to achieve more homogeneous mold filling while minimizing powder–binder separation and oxidation risks. This conceptual shift redefines the injection stage from a mechanically dominated operation to a thermally and atmospherically controlled process environment.

The gas-assisted powder injection molding (GAMIM) approach discussed in this chapter is based on this fundamental rethinking of the injection mechanism. Rather than relying on screw or piston-driven pressure, the system employs high-pressure inert gas to transfer a thermally conditioned feedstock

into the mold cavity. The methodology has been systematically developed and validated through a series of experimental studies addressing feedstock formulation, molding behavior, sintering response, and functional performance in both metallic and biomaterial systems (Cicek, Sun, Turen, & Ahlatci, 2021; Çiçek & Sun, 2023). These studies demonstrate that gas-assisted injection can effectively preserve feedstock homogeneity and promote controlled microstructural evolution during sintering.

Experimental investigations on magnesium-based alloys have shown that the GAMIM concept enables stable shaping and sintering behavior, leading to well-developed neck formation and refined microstructures despite the intrinsic reactivity of magnesium powders (Cicek et al., 2021). In parallel, applications to 316L stainless steel systems have revealed favorable densification behavior, improved corrosion resistance in simulated body fluids, and high cell viability, confirming the suitability of the process for biomedical applications (Çiçek & Sun, 2023). These findings highlight that the injection strategy itself can act as a key microstructure-controlling parameter, rather than a passive processing step.

Accordingly, this chapter presents a combined review and experimental synthesis of gas-assisted powder injection molding systems, with a particular emphasis on feedstock behavior, injection mechanics, sintering evolution, and functional outcomes. By integrating classical PIM literature with recent experimental insights, the chapter aims to provide a coherent framework for understanding how alternative injection concepts can expand the applicability of PIM to reactive metals and advanced biomaterial systems. The discussion is structured to bridge fundamental principles with practical system design, offering guidance for both academic research and future industrial implementation.

2. Fundamentals of PIM and Material–Process Interactions

PIM is a well-established manufacturing technique that enables the production of complex-shaped metallic components by combining powder metallurgy with injection molding principles. The process consists of feedstock preparation, injection molding, debinding, and sintering stages, all of which collectively determine the final microstructure and performance of the material. In conventional PIM systems, the injection stage is typically driven by mechanical pressure, and this stage plays a decisive role in defining powder distribution, green part integrity, and subsequent densification behavior during sintering (German, 1984, 1990; German et al., 1991).

Feedstock formulation is a critical factor governing the success of PIM processing. Multicomponent binder systems, particularly PEG–PMMA-based formulations, have been widely investigated due to their favorable flow characteristics and solvent-debinding capability. Studies have shown that appropriate control of binder composition and powder loading enhances green part stability and reduces defect formation during debinding and sintering (Bakan et al., 1998; Omar et al., 2001). Nevertheless, even with optimized feedstocks, non-uniform flow and powder–binder separation may occur during injection, especially under high shear conditions.

The type and application mode of pressure during injection have therefore gained increasing attention in recent studies. Mechanical pressure generated by screws or hydraulic systems can induce shear-related inhomogeneities, leading to local density gradients and microstructural variations in molded

parts. Experimental investigations on stainless steel feedstocks have demonstrated that pressure type significantly influences flow behavior, green part quality, and sintered Microstructure (Nayak, Ramesh, Desai, & Samanta, 2018; Türen, 2017). These effects become particularly critical when processing fine powders or systems with narrow processing windows.

Challenges associated with injection-induced inhomogeneity are further amplified in reactive and biomedical material systems, such as magnesium alloys and Mg–Ca-based materials. These materials are highly sensitive to oxygen pickup, residual porosity, and microstructural discontinuities, all of which directly affect mechanical integrity and corrosion behavior (Makkar et al., 2018; Sezer, Evis, Kayhan, Tahmasebifar, & Koc, 2018). Consequently, the injection stage should not be regarded solely as a shaping operation, but rather as a key microstructure-defining step within the overall PIM process. This understanding forms the basis for alternative injection concepts aimed at improving feedstock stability and extending PIM applicability to advanced and reactive material systems.

3. Concept of GAMIM

GAMIM has been developed as an alternative injection strategy to overcome the limitations associated with mechanically driven PIM systems. In contrast to conventional screw- or hydraulically actuated injection, the GAMIM approach employs high-pressure inert gas to transfer a thermally conditioned, gel-phase feedstock into the mold cavity. By decoupling feedstock flow from direct mechanical shear, this system aims to preserve powder–binder homogeneity during mold filling and reduce segregation effects that are commonly observed in traditional injection stages (Türen, 2017).

The fundamental operating principle of the GAMIM system is based on controlling the feedstock in a semi-fluid state under a precisely regulated thermal environment, followed by gas-driven injection under inert atmosphere conditions. The use of inert gas not only provides the driving force for mold filling but also limits oxygen exposure during injection, which is particularly critical for reactive materials such as magnesium alloys. Previous studies on magnesium-based and Mg–Ca systems have demonstrated that minimizing oxidation and flow-induced defects at the injection stage contributes to more stable sintering behavior and refined microstructural evolution (Makkar et al., 2018; Sezer et al., 2018).

From a processing perspective, GAMIM redefines the role of pressure in PIM by shifting it from a mechanically applied parameter to an atmospherically controlled process variable. This transition allows for more uniform pressure distribution throughout the feedstock, reducing localized stress concentrations and binder migration. Similar sensitivities to pressure mode have been reported in stainless steel feedstocks, where the nature of applied pressure significantly influences green part density and sintered microstructure (Nayak et al., 2018). Accordingly, the GAMIM concept offers a more stable and reproducible injection environment for materials with narrow processing windows.

Overall, the GAMIM system represents a conceptual advancement rather than a mere mechanical modification of conventional PIM equipment. By integrating thermal control, inert atmosphere, and gas-driven injection into a single process framework, the system provides a robust platform for processing reactive metals and biomedical materials. This approach establishes a direct link between injection mechanics and microstructural control, forming the basis for the experimental methodologies and material systems discussed in the subsequent sections.

4. Experimental Methodology and Processing Route

The experimental methodology adopted in this study is based on the classical Powder Injection Molding framework, modified by integrating a gas-assisted injection strategy at the molding stage. Previous investigations have shown that the injection mechanism plays a critical role in defining feedstock homogeneity, green part integrity, and sintering response, particularly in stainless steel and reactive metal systems (Türen, 2017; Nayak et al., 2018). Building on these findings, the present approach treats the injection stage as a microstructure-defining process parameter rather than a purely mechanical shaping operation, as demonstrated in earlier studies conducted by the authors on gas-assisted PIM systems (Cicek et al., 2021).

Feedstock preparation was carried out using fine metallic powders combined with PEG–PMMA-based multicomponent binder systems. This binder formulation has been widely reported to provide favorable flow behavior and effective solvent debinding while maintaining sufficient green strength (Bakır et al., 1998; Omar et al., 2001). In the authors' previous studies, PEG–PMMA feedstocks were shown to ensure homogeneous powder distribution and stable molding behavior when processed under controlled thermal conditions, forming a reliable basis for both stainless steel and magnesium-based material systems (Cicek et al., 2021; Cicek et al., 2023). Particular attention was paid to minimizing powder–binder separation during mixing and molding, as this effect has been identified as a major source of sintering-related defects.

Injection molding was performed using the GAMIM system developed and experimentally validated by the authors. As schematically illustrated in Figure 1, the feedstock is first heated within a dedicated chamber to reach a stable gel-like state under controlled temperature conditions. Subsequently, the conditioned feedstock is transferred into the mold cavity by the application of high-pressure inert gas, which acts as the driving force for injection while minimizing mechanical shear and oxidation during mold filling. Compared to conventional mechanically driven injection, this approach reduces shear-induced segregation and limits oxidation during mold filling. The effectiveness of this injection strategy has been previously demonstrated for magnesium-based alloys and Mg–Ca systems, where improved flow stability and microstructural uniformity were achieved despite the high reactivity of the powders (Cicek et al., 2021; Makkar et al., 2018; Sezer et al., 2018). Similar advantages have also been reported for stainless steel feedstocks, where pressure application mode directly influences green part density and sintering behavior (Türen, 2017; Nayak et al., 2018).

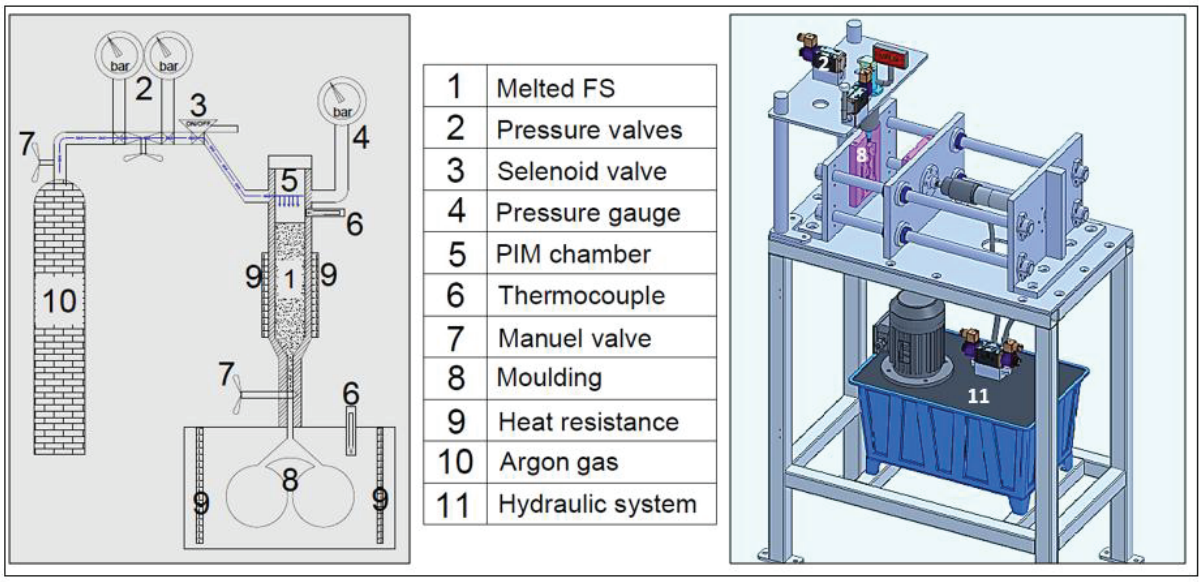

Figure 1. General layout of GAMIM system illustrating the feedstock heating chamber, inert gas-assisted injection stage, and modified mold unit.

Following injection, the molded green parts were subjected to conventional debinding and sintering procedures appropriate for the investigated material systems. Sintering parameters were selected based on prior experimental studies conducted by the authors, which demonstrated the strong dependence of densification, grain development, and phase evolution on the initial injection-induced homogeneity (Cicek et al., 2021; Cicek et al., 2023). This processing route enabled a systematic assessment of the influence of gas-assisted injection on the transition from feedstock to consolidated metallic structure, providing a consistent experimental foundation for the microstructural and functional analyses discussed in the following sections.

5. Sintering Behavior and Microstructural Evolution

Sintering represents the most critical stage in the Powder Injection Molding route, during which the spatial powder arrangement established during injection is transformed into a continuous metallic structure. The effectiveness of this stage is strongly governed by the homogeneity of the green part, which in turn is influenced by the injection strategy. In the authors' previous studies, it was demonstrated that gas-assisted injection leads to more uniform powder distribution, thereby promoting stable densification and predictable microstructural evolution during sintering (Cicek et al., 2021; Cicek et al., 2023).

Experimental investigations on magnesium-based and Mg–Ca alloy systems processed via the GAMIM approach revealed classical powder metallurgy sintering stages, including initial particle contact, neck formation, and grain coalescence. As sintering temperature and duration increased, a gradual transition from point contact to well-defined grain boundaries was observed. In particular, controlled sintering conditions enabled the formation of Mg_2Ca phases at grain boundaries without excessive oxidation, confirming that the gas-assisted injection stage contributes to maintaining a favorable chemical and structural environment for reactive materials (Cicek et al., 2021). These findings highlight the strong coupling between injection-induced homogeneity and sintering-driven microstructural development.

Similar trends were observed in biomedical-grade 316L stainless steel systems produced using the same gas-assisted injection methodology. The authors reported that improved green part uniformity resulted in enhanced densification behavior and more consistent grain structures after sintering. Variations in sintering temperature directly affected porosity reduction and grain growth, while the absence of severe injection-induced defects allowed the sintering process to proceed in a controlled and reproducible manner (Cicek et al., 2023). These results indicate that the benefits of gas-assisted injection are not limited to reactive alloys but are also applicable to conventional biomaterial systems.

Overall, the sintering behavior observed in GAMIM-processed materials confirms that the injection stage plays a decisive role in defining microstructural evolution. By minimizing segregation, oxidation, and local density gradients during molding, gas-assisted injection establishes favorable initial conditions for sintering. Consequently, the resulting microstructures exhibit improved continuity and stability, providing a robust foundation for achieving desirable mechanical and functional properties in both magnesium-based and stainless steel materials.

6. Functional Performance and Material Response

The functional performance of PIM-produced components is directly linked to the integrity of the microstructure developed during injection and sintering stages. Parameters such as density, hardness, corrosion resistance, and biological response are particularly sensitive to residual porosity, oxide content, and grain boundary continuity. In the authors' previous studies, it was clearly demonstrated that gas-assisted injection contributes to improved green part homogeneity, which translates into enhanced densification and more stable functional behavior after sintering (Cicek et al., 2021; Cicek et al., 2023).

For magnesium-based and Mg–Ca alloy systems, gas-assisted injection followed by controlled sintering resulted in metallic structures with well-developed grain boundaries and limited oxide presence. The authors reported that adequate densification and phase formation, particularly the controlled appearance of Mg_2Ca phases, led to measurable improvements in hardness while preserving structural continuity (Cicek et al., 2021). These outcomes are significant for reactive alloys, where excessive porosity or oxide formation typically results in mechanical degradation and unstable corrosion behavior. The observed results confirm that the GAMIM approach enables a more reliable transition from green part to functional metallic structure in magnesium-based systems.

In biomedical-grade 316L stainless steel produced via the same processing route, functional performance was evaluated in terms of density, hardness, and corrosion behavior in simulated physiological environments. The authors' findings indicated that increased sintering temperature promoted higher density values and improved hardness, while uniform microstructural development reduced localized corrosion susceptibility (Cicek et al., 2023). Potentiodynamic corrosion tests conducted in artificial body solutions further revealed low corrosion rates and stable electrochemical behavior, demonstrating that gas-assisted injection does not compromise, and may even enhance, the corrosion resistance of sintered 316L components.

Beyond mechanical and electrochemical performance, biological response represents a critical criterion for biomaterial applications. Cytotoxicity assessments performed on sintered 316L samples produced by the GAMIM method showed high cell viability, confirming the biocompatibility of the

material and the absence of harmful residuals associated with the modified injection process (Cicek et al., 2023). Taken together, these results highlight that gas-assisted powder injection molding supports not only microstructural control but also functional reliability, positioning the GAMIM approach as a promising processing route for both reactive alloys and biomedical materials.

7. Conclusions and Outlook

This chapter has presented a combined review and experimental synthesis of GAMIM as an alternative processing route to conventional PIM systems. By reconsidering the injection stage as a microstructure-defining process rather than a purely mechanical shaping operation, the GAMIM concept addresses critical limitations associated with shear-induced segregation, oxidation, and flow instability. The experimental findings discussed throughout the chapter demonstrate that gas-assisted injection provides a more homogeneous green part structure, which serves as a stable foundation for controlled sintering and reliable functional performance (Cicek et al., 2021; Cicek et al., 2023).

The results obtained for magnesium-based and Mg–Ca alloy systems highlight the particular suitability of the GAMIM approach for reactive materials. Improved powder distribution during injection enabled predictable sintering behavior, well-developed grain structures, and controlled phase formation without excessive oxidation. These outcomes confirm that modifying the injection mechanism can significantly expand the applicability of PIM to materials traditionally considered challenging due to their chemical reactivity and narrow processing windows (Cicek et al., 2021).

Similarly, investigations on biomedical-grade 316L stainless steel demonstrated that gas-assisted injection does not compromise densification, corrosion resistance, or biocompatibility. On the contrary, the observed improvements in microstructural uniformity and functional response suggest that GAMIM offers a robust and reproducible processing route for biomedical applications where structural integrity and biological safety are critical (Cicek et al., 2023). The consistency of these results across different material systems underscores the generality of the proposed injection strategy.

From an outlook perspective, gas-assisted powder injection molding represents a promising platform for the future development of advanced PIM technologies. Its inherent compatibility with reactive metals, biomaterials, and fine powder systems positions GAMIM as a versatile alternative to mechanically driven injection methods. Further optimization of process parameters and system design may enable broader industrial adoption, particularly in applications requiring complex geometries, controlled microstructures, and high functional reliability. As such, the GAMIM concept offers a forward-looking pathway for extending the boundaries of powder injection molding beyond conventional material and processing limits.

Acknowledgements

The authors would like to acknowledge that the experimental framework and scientific background of this chapter were derived from the doctoral thesis of the corresponding author. The authors also gratefully acknowledge the financial support provided by the Karabuk University Scientific Research Projects Unit under Project No. FDK-2019-2106, which contributed to the completion of this study.

References

Anderson, K., Groza, J., Fendorf, M., & Echer, C. (1999). Surface oxide debonding in field assisted powder sintering. *MAT SCI ENG A-STRUCT, 270*(2), 278. doi:https://doi.org/10.1016/S0921-5093(99)00197-5

Bakan, H., Jumadi, Y., Messer, P., Davies, H., & Ellis, B. (1998). Study of processing parameters for MIM feedstock based on composite PEG-PMMA binder. *Powder Metall., 41*(4), 289. doi:https://doi.org/10.1179/pom.1998.41.4.289

Cicek, B., Sun, Y., Turen, Y., & Ahlatci, H. (2021). Applicability of different powder and polymer recipes in a new design powder injection molding system. *Journal of Polymer Engineering, 41*(4), 299-309.

Çiçek, B., & Sun, Y. (2023). Material Production and the effect of the SySteM on BiocoMPatiBility in the Modified Metal injection Method. *Archives of Metallurgy and Materials, 68*.

Friedrich, H., & Schumann, S. (2001). Research for a "new age of magnesium" in the automotive industry. *Journal of Materials Processing Technology, 117*(3), 276. doi:https://doi.org/10.1016/S0924-0136(01)00780-4

German, R. M. (1984). *Powder Metallurgy Science*. Wiley, USA: Metal Powder Indust Feder.

German, R. M. (1990). *Powder Injection Molding*. New Jersey, USA: Metal Powder Indust Feder.

German, R. M., Hens, K. F., & Lin, S.-T. P. (1991). Key issues in powder injection molding. *Am. Ceram. Soc. Bull., 70*(8), 1294-1302.

Hartwig, T., Veltl, G., Petzoldt, F., Kunze, H., Scholl, R., & Kieback, B. (1998). Powders for metal injection molding. *J. Eur. Ceram. Soc., 18*(9), 1211. doi:https://doi.org/10.1016/S0955-2219(98)00044-2

Li, S.-l., Huang, B.-y., Qu, X.-h., & Li, Y.-m. (1999). Solvent de-binding of water-soluble binder in powder injection moulding. *Transactions of the Nonferrous Metals Society of China, 9*(3), 578.

Makkar, P., Sarkar, S. K., Padalhin, A. R., Moon, B.-G., Lee, Y. S., & Lee, B. T. (2018). In vitro and in vivo assessment of biomedical Mg–Ca alloys for bone implant applications. *J Appl Biomater Funct Mater, 16*(3), 126. doi:https://doi.org/10.1177/2280800017750359

Nayak, C. V., Ramesh, M., Desai, V., & Samanta, S. K. (2018). Fabrication of stainless steel based composite by metal injection moulding. *Mater. Today, 5*(2), 6805. doi:https://doi.org/10.1016/j.matpr.2017.11.340

Omar, M., Davies, H., Messer, P., & Ellis, B. (2001). The influence of PMMA content on the properties of 316L stainless steel MIM compact. *J. Mater. Process Tech., 113*(1-3), 477. doi:https://doi.org/10.1016/S0924-0136(01)00641-0

Rak, Z. (1998). New trends in powder injection moulding. *Powder Metall. Met. C+, 38*(3-4), 126. doi:https://doi.org/10.1007/BF02676037

Sezer, N., Evis, Z., Kayhan, S. M., Tahmasebifar, A., & Koc, M. (2018). Review of magnesium-based biomaterials and their applications. *J. Magnes. Alloy.*, 23-36. doi:https://doi.org/10.1016/j.jma.2018.02.003

Türen, Y. (2017). Influence of Pressure Type on Powder Injection Moulding of Stainless Steel (316L) Powder. *Hitite J. Sci. Eng., 4*(2), 85. doi:https://doi.org/10.17350/HJSE19030000053

Wolff, M., Ebel, T., & Dahms, M. (2010). Sintering of magnesium. *Advanced engineering materials, 12*(9), 829. doi:https://doi.org/10.1002/adem.201000038

Yang, W.-W., Yang, K.-Y., Wang, M.-C., & Hon, M.-H. (2003). Solvent debinding mechanism for alumina injection molded compacts with water-soluble binders. *Ceramics International, 29*(7), 745. doi:10.1016/S0272-8842(02)00226-2

Zheng, Y., Gu, X., Xi, Y., & Chai, D. (2010). In vitro degradation and cytotoxicity of Mg/Ca composites produced by powder metallurgy. *Acta biomaterialia, 6*(5), 1783.

Chapter 3

USE OF BORON MINING WASTES IN GEOPOLYMER BINDERS: CHEMICAL FUNDAMENTALS, MIX DESIGN STRATEGIES, AND ENGINEERING APPLICATIONS

Kemal Şahbudak[1], Birol Yazarlı[2]

1 Doç.Dr. Sivas Cumhuriyet Üniversitesi, Mühendislik Fakültesi, Metalürji ve Malzeme Mühendisliği Bölümü, Üretim Metalürjisi Anabilim Dalı, Sivas, 000-0003-4853-6843.
2 Öğr.Gör.Yozgat BOZOK Üniversitesi, Akdağmadeni Meslek Yüksekokulu,Yozgat, 000-0002-9266-3682.

1. Introduction

The increasing global demand for sustainable infrastructure and low-carbon construction materials has necessitated a critical reassessment of the environmental impacts associated with traditional binder technologies. Currently, the construction sector accounts for approximately 38% of global CO_2 emissions, while the cement industry alone contributes 7–8% of total anthropogenic emissions (Scrivener et al., 2018, as cited in Zhang et al., 2023). The production of Portland cement—requiring high process temperatures and generating 800–900 kg CO_2 per ton of clinker—poses significant challenges to long-term sustainability targets. Consequently, the development of alternative binders capable of reducing carbon footprints, valorizing industrial by-products, and delivering performance comparable to cement-based systems has become a strategic research priority.

Alkali-activated geopolymer binders have emerged as promising candidates due to their low environmental footprint and superior mechanical and thermal performance (Provis, 2018, as cited in Hussein et al., 2021). Geopolymerization is a multi-step chemical process involving the dissolution of aluminosilicate precursors in an alkaline medium, followed by the formation of reactive monomeric species and their subsequent polycondensation into three-dimensional N–A–S–H or C–A–S–H gel frameworks (Davidovits, 2020, as cited in Kaya & Demir, 2022). The resulting geopolymers exhibit excellent thermal stability, chemical resistance, low permeability, and long-term durability, positioning them as viable alternatives to conventional cementitious materials (Bernal et al., 2014, as cited in Wang et al., 2020a).

Türkiye holds approximately 73% of the world's boron reserves, leading to the annual generation of 2–3 million tons of by-products such as colemanite, tincal, ulexite, and boron sludge (Gür et al., 2020, as cited in Karahan & Yıldız, 2022). During alkali activation, boron species are transformed into BO_3 and BO_4 structural units, which modify the chemical architecture of the geopolymer gel network. This transformation can exert both reinforcing and, under certain conditions, weakening effects on the geopolymer matrix (Hajimohammadi et al., 2017). Low boron concentrations generally enhance strength, whereas higher doses have been associated with increased porosity and microstructural deterioration (Wang et al., 2020c). In addition, synergistic interactions between boron and MgO promote the formation of B–Mg–Si–Al hybrid gel structures, which further improve mechanical performance (Abdullah, Yong, Zamri, & Abd Razak, 2022b).

This chapter provides a comprehensive framework for understanding the use of boron-containing wastes in geopolymer binders—from their chemical composition and reaction mechanisms to mix-design considerations, performance characteristics, and engineering applications. The goal is to demonstrate that boron wastes are not merely industrial by-products but can serve as value-added components within geopolymer systems when scientifically engineered.

2. Chemical and Mineralogical Characteristics of Boron Wastes

By-products generated from boron mining and refining processes—such as colemanite, ulexite, tincal, and boron precipitation sludge—exhibit highly heterogeneous chemical and mineralogical characteristics. Owing to these features, they fall within the category of reactive precursor materials that can be effectively utilized in geopolymer production. Türkiye's dominance in global boron reserves results in the generation of these wastes in large quantities each year, making their reuse in sustainable material systems strategically important for both environmental management and materials science (Gür, Acar, & Yalçın, 2020).

Although the chemical composition of boron wastes varies significantly, they typically contain 8–26% B_2O_3, 15–25% CaO, and 10–28% SiO_2, with MgO, Na_2O, and Al_2O_3 present in smaller quantities (Kaya, Ersöz, & Uzun, 2023). The B_2O_3 content governs the formation of BO_3 and BO_4 units during

alkali activation, directly influencing the chemical equilibrium of polycondensation reactions (Hajimohammadi et al., 2017). Meanwhile, the CaO and MgO fractions contribute to the development of hybrid C–A–S–H and B–A–S–H gel phases, which play a critical role in defining the hardening behavior of the binder (Abdullah et al., 2022b). The oxide compositions reported for various types of boron waste—summarized in Table 2.1—demonstrate that these differences have a significant impact on the alkali activation potential of each material (Aydın & Kızıltepe, 2019; Benk et al., 2013; Alkan et al., 2017; Serdar & Cavit, 2019; Tayibi et al., 2009).

Table 2.1. Typical Chemical and Mineralogical Composition of Boron Mining Wastes

Waste Type	**Major Minerals**	**Chemical Composition (wt%)**	**Reference**
Colemanite waste	Colemanite ($Ca_2B_6O_{11}\cdot5H_2O$), calcite, quartz, clay minerals	SiO_2: 8–20; Al_2O_3: 1–4; Fe_2O_3: 0.5–2; CaO: 20–30; MgO: 1–4; B_2O_3: 15–25	Aydın & Kızıltepe (2019)
Ulexite waste	Ulexite ($NaCaB_5O_9\cdot8H_2O$), calcite, dolomite, quartz	SiO_2: 5–15; Al_2O_3: 1–3; Fe_2O_3: 0.5–1; CaO: 15–25; Na_2O: 5–12; B_2O_3: 18–28	Serdar & Cavit (2019)
Tincal (borax) waste	Tincal ($Na_2B_4O_7\cdot10H_2O$), thenardite, halite, quartz	SiO_2: 2–10; Al_2O_3: 0.5–2; Fe_2O_3: 0.2–1; CaO: 1–5; Na_2O: 10–18; B_2O_3: 10–20	Tayibi et al. (2009)
Boric acid production waste	Decomposition products of colemanite and ulexite, amorphous boron oxide, calcite	SiO_2: 10–25; Al_2O_3: 1–4; Fe_2O_3: 0.5–2; CaO: 15–30; B_2O_3: 5–12	Alkan et al. (2017)
Boron precipitation sludge	Clay minerals, calcite, colemanite/ulexite particles	SiO_2: 20–35; Al_2O_3: 4–8; Fe_2O_3: 1–3; CaO: 10–20; B_2O_3: 3–8	Benk et al. (2013)

Mineralogically, boron wastes contain a complex mixture of hydrated borates (colemanite, borax, ulexite), Ca–B–O and Mg–B–O phases, along with quartz and carbonate impurities. The rapid dissolution of hydrated borate phases in highly alkaline environments releases BO_3^{3-} and BO_4^{5-} units, significantly influencing the dissolution kinetics that dominate the initial stage of geopolymerization (Hajimohammadi et al., 2017). Amorphous and semi-crystalline borate phases generally exhibit higher reactivity, whereas crystalline phases dissolve more slowly, requiring careful consideration of waste dosage and phase composition during mix design (Wang et al., 2020b).

The dissolution behavior of boron wastes in alkaline media accelerates as NaOH concentration increases. This enhances the $BO_3 \rightarrow BO_4$ transformation, altering solution chemistry and directly shaping the direction of polycondensation. However, excessive dissolution—particularly in wastes with high B_2O_3 content—may lead to microvoid formation and discontinuities in the gel matrix, ultimately compromising material integrity (Kaya et al., 2023). Therefore, the effective use of boron wastes in geopolymer synthesis requires a holistic assessment of both chemical composition and phase reactivity.

Morphological characterization further reveals that the reactivity potential of boron wastes is closely linked to their surface properties. SEM images (Figure 2.1) show that borax particles exhibit irregular,

fractured, and porous morphologies, whereas magnesium oxide particles possess a more compact texture. These contrasting surface features directly affect dissolution rates and reactive surface areas, which are key parameters controlling the progression of geopolymerization (Abdullah & Rahman, 2021). The porous structure of borax enhances dissolution, while the denser morphology of MgO enables slower dissolution and can act as a pH-modulating component within the system.

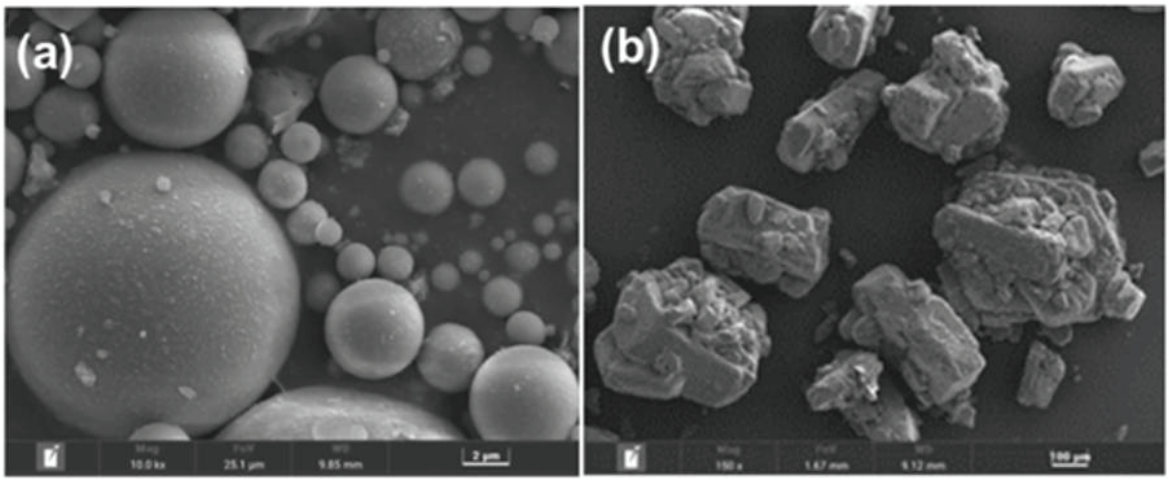

Figure 2.1. SEM Images of Boron Waste Materials (a) Fly ash (FA), (b) Borax Source: Abdullah & Rahman (2021)

Understanding the chemical and mineralogical characteristics of boron wastes is therefore essential for elucidating their dissolution behavior in alkaline environments and their influence on BO_3/BO_4 transformations, polycondensation mechanisms, and overall geopolymer performance.

3. Effects of Boron on Geopolymerization

In boron-containing systems, the mechanism of geopolymerization is governed by a complex reaction network in which sequential chemical processes—dissolution, polycondensation, and gel formation—interact with one another. During alkali activation, borate species released from boron-bearing minerals directly influence the pH balance of the medium, the dissolution rate, and the chemical composition of the developing N–A–S–H or C–A–S–H gel phases. Therefore, boron should not be regarded merely as an inert mineral additive but rather as an active chemical modifier that governs the reaction mechanism (Hajimohammadi et al., 2017).

Monitoring mineralogical evolution is critical for understanding boron's dissolution behavior and reactivity potential. As shown in the XRD pattern in Figure 3.1, natural phases such as tinkalkonite, quartz, dolomite, and calcite dominate before alkali fusion, whereas after activation, the system transitions into more reactive phases including sodium peroxide, magnesium oxide, merwinite, and sodium magnesium silicate (Kızıltepe, Yüksel, & Aydın, 2025, Fig. 4).

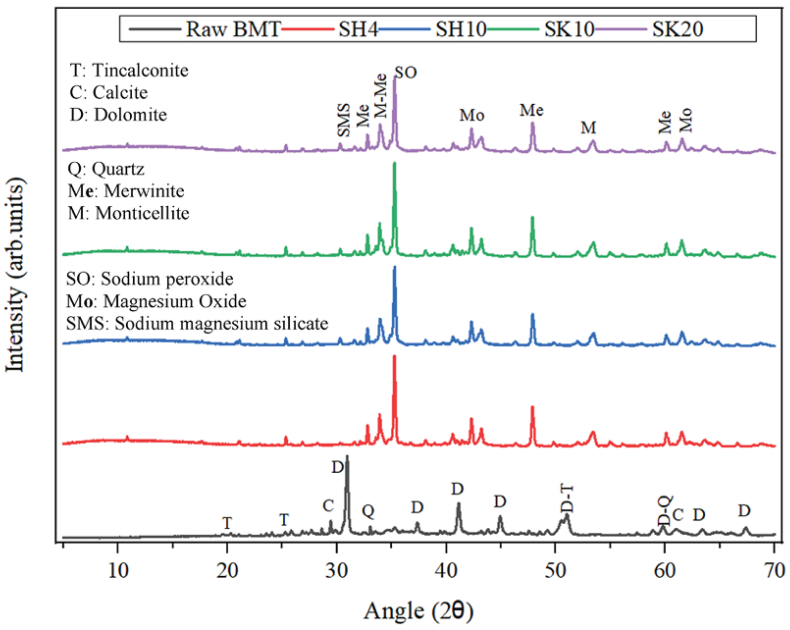

Figure 3.1. Phase transformation after alkali fusion (Kızıltepe et al., 2025).

The emergence of these new phases demonstrates that the reactivity of boron-bearing minerals increases markedly when exposed to alkaline solutions, accelerating the dissolution stage—the first step of geopolymerization. Borate species released into the solution not only affect the dissolution rate but also modify viscosity and ionic composition, thereby governing the direction of polycondensation reactions.

Thermal analyses further support this chemical restructuring. In TG/DTA curves, mass losses observed between 30–500 °C correspond to the removal of hydration and structural water, while abrupt losses between 500–700 °C are attributed to the decomposition of carbonate phases and the transition of borate species into anhydrous forms (Figure 3.2). These temperature-dependent changes reveal chemical transformations within boron-bearing minerals that enhance reactivity and directly influence the composition of the gel structure formed during the polycondensation stage (Kızıltepe et al., 2025, Fig. 3).

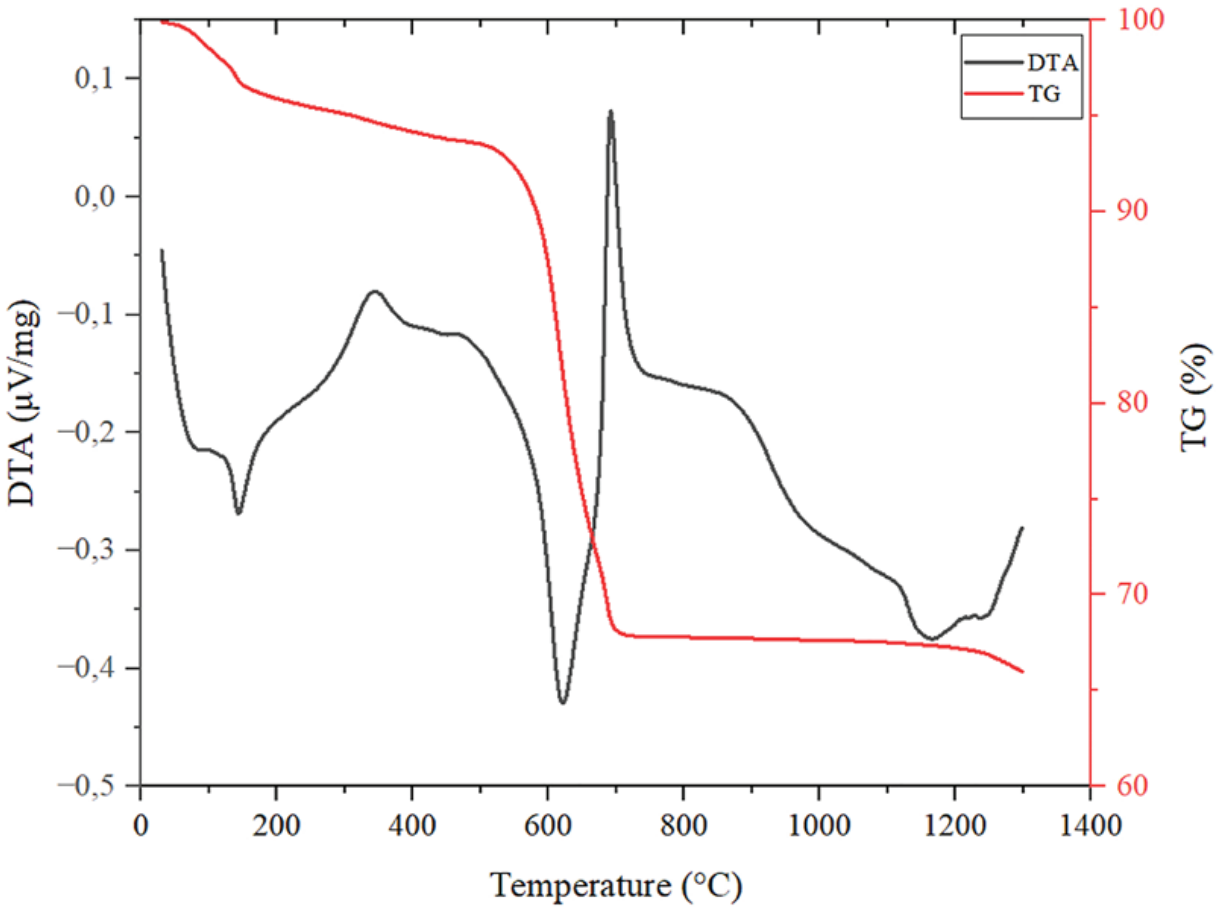

Figure 3.2. TG/DTA analysis of boron wastes (Kızıltepe et al., 2025).

During the polycondensation phase, the effect of boron is largely associated with the relative proportions of BO_3 and BO_4 structural units. Trigonal BO_3 groups weaken oxygen bridges within the geopolymer network and reduce bond density, whereas tetrahedral BO_4 units strengthen the three-dimensional framework, producing a denser polymer matrix. At low boron dosages, this can enhance gel connectivity; however, higher levels promote microvoid formation, softening the gel and reducing mechanical performance (Wang et al., 2020). The influence is not limited to structural bonding; it also extends to dissolution rate, polycondensation tendencies, and the stability of the resulting gel phases.

When boron and MgO are used together, the mechanism follows a different pathway. MgO hydration produces $Mg(OH)_2$, which increases local pH, counteracting boron's retardation effect, while forming complex structures with borate species that help regulate reaction progression. This interaction promotes the development of B–Mg–Si–Al hybrid gels, producing a denser matrix and significantly enhancing mechanical performance. The synergistic effect of MgO and boron in improving geopolymer matrix density and strength has been verified in various studies (Abdullah et al., 2022b).

Overall, boron does not act merely as an additional component in the geopolymerization process—it actively directs the entire reaction sequence, from solution chemistry to gel formation. The shifts in phase composition, variations in dissolution behavior, adjustments in polycondensation pathways, and resulting microstructural evolution position boron as a powerful chemical regulator in geopolymer systems. The effective utilization of boron wastes in geopolymers therefore depends on a detailed understanding of the geopolymerization mechanism and the precise control of boron's multifaceted effects during mix design.

4. Mix Design in Boron Waste–Incorporated Geopolymers

Mix design in boron waste–incorporated geopolymers requires a more complex optimization process compared to conventional alkali-activated systems, primarily because boron-containing species exert multidimensional effects on geopolymerization. The dissolution of borate species under high-alkalinity conditions directly influences dissolution kinetics, polycondensation equilibrium, and gel formation mechanisms, thereby restructuring the overall reaction network. For this reason, variables such as NaOH molarity, sodium silicate/NaOH ratio, solid-to-liquid ratio (S/L), alkali activator-to-binder ratio (AAS/FA), boron waste content, and MgO addition must be evaluated collectively (Hajimohammadi et al., 2017).

The AAS/FA ratio is one of the key parameters determining reactivity and bond formation rate in geopolymer systems. Due to boron's ability to slow dissolution and buffer alkalinity, this ratio must be controlled within a narrower window in boron-containing mixtures. Literature indicates that an AAS/FA ratio of 0.40–0.55 optimizes both workability and strength (He et al., 2025).

Increasing NaOH concentration accelerates dissolution and promotes BO_4 formation; however, concentrations above 12 M may weaken the gel structure (Wang et al., 2020b). Maintaining the sodium silicate/NaOH ratio between 1.2 and 1.5 supports balanced reaction progression (Provis, 2018). Boron waste content is one of the most sensitive components of mix design. Low boron levels (5–10 wt%) promote the development of BO_4 units, resulting in a more compact gel network and increased mechanical strength. Conversely, additions exceeding 15% cause BO_3 units to dominate, leading to increased microvoid formation and strength reduction (Hajimohammadi et al., 2017; Kaya et al., 2023).

MgO addition acts as a secondary activator that compensates for boron's retarding effects. Through the formation of $Mg(OH)_2$, local pH increases, and Mg^{2+} ions form complex bonds with borate and silicate species, promoting the development of dense B–Mg–Si–Al gel phases. Studies demonstrate that the combination of 5% boron + 5% MgO yields optimal strength, confirming the critical role of the boron–MgO synergy in mix design (Abdullah et al., 2022a).

The additional water released during the dissolution of boron species and the associated increase in viscosity require recalibration of the solid-to-liquid ratio. While S/L ratios between 0.50 and 0.60 are suitable for boron-free geopolymers, the optimal range shifts to 0.55–0.70 in boron-containing systems (Wang et al., 2020c).

Taguchi-based optimization studies, which evaluate multivariable interactions simultaneously, support these trends. These analyses identify NaOH molarity as the most influential parameter, followed by the SS/NaOH ratio, silica fume content, and boron concentration. The resulting optimum mix design parameters are summarized in Table 4.1 (He et al., 2025).

Table 4.1. Optimum Mix Design Parameters for Boron Waste–Incorporated Geopolymers

Design Parameter	Recommended Range	Reference
NaOH molarity	10–12 M	(Hajimohammadi et al., 2017; Wang et al., 2020b)
SS/NaOH ratio	1.2–1.5	(Provis, 2018)
Boron waste content	5–10%	(Hajimohammadi et al., 2017; Kaya et al., 2023)
MgO addition	3–8%	(Abdullah et al., 2022a)
Silica fume	5–15%	(Karlıoğlu-Kaya & Onur, 2025)
AAS/FA ratio	0.40–0.55	(He et al., 2025)
S/L ratio	0.55–0.70	(Wang et al., 2020c)

Overall, the findings indicate that mix design in boron-containing geopolymers depends not on a single parameter but on a network of interrelated variables—including dissolution equilibria, gel formation dynamics, viscosity control, and reaction kinetics. Therefore, achieving optimum performance requires a balanced and holistic approach to selecting mix design parameters.

5. Performance Characteristics of Boron Waste–Incorporated Geopolymers

The performance of boron waste–incorporated geopolymers depends on the dissolution behavior of boron-containing species, the balance between BO_3 and BO_4 units, and the manner in which B–O–Si bonds formed during polycondensation reorganize the matrix structure. The geopolymerization mechanism summarized in Figure 5.1 (Provis, 2018; Davidovits, 2020) clearly demonstrates why boron generates multidimensional effects on both fresh and hardened properties. While boron slows dissolution and extends setting time, the development of BO_4 units contributes to a denser gel network and enhanced strength; in contrast, BO_3-dominated speciation leads to microstructural discontinuities and strength reduction (Hajimohammadi et al., 2017). Therefore, the performance of boron-containing geopolymers is governed by the simultaneous optimization of chemical processes and microstructural evolution.

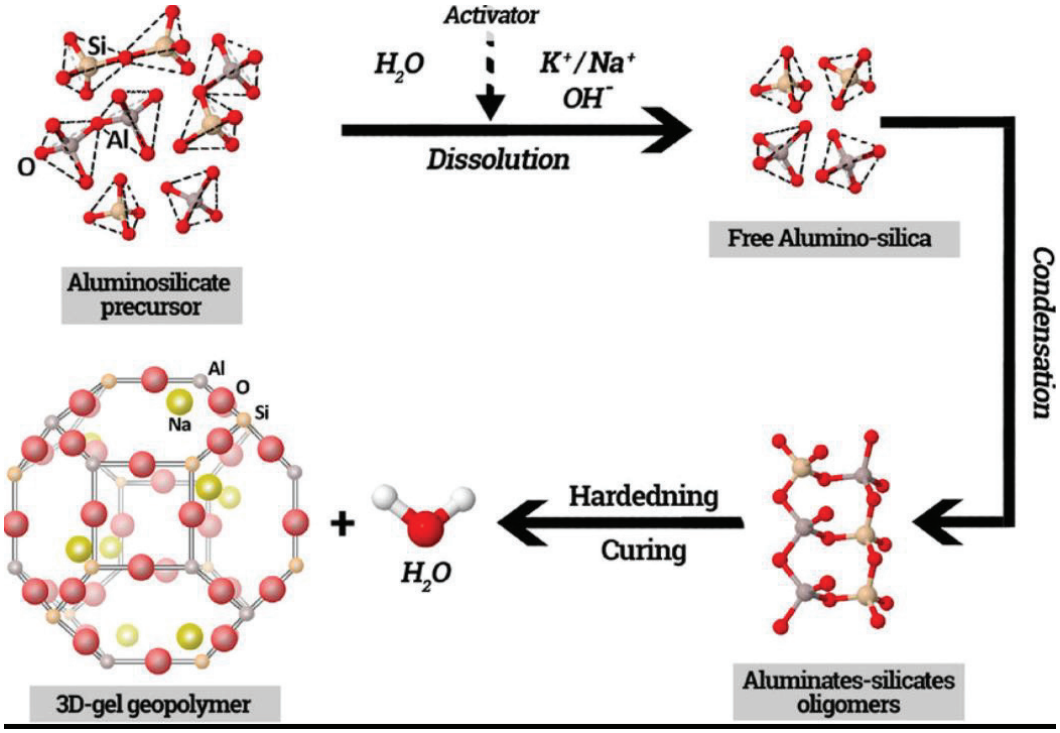

Figure 5.1. Schematic representation of the geopolymerization mechanism.

The incorporation of boron into geopolymer systems causes significant delays in setting due to the slow dissolution of hydrated borate minerals in alkaline solutions. Borate species buffer the alkalinity of the medium, reducing the dissolution rate of aluminosilicates and extending setting times as boron dosage increases. At 10–15% boron content, the reaction rate decreases substantially, and in some mixtures, complete hardening may not occur (He et al., 2025). The addition of MgO promotes the formation of $Mg(OH)_2$ through hydration, elevating local pH and partially counteracting boron's retarding effect—thereby enhancing early-stage reaction capacity (Abdullah et al., 2022). The interaction between MgO and boron is considered a key design parameter governing early reaction behavior and setting performance.

The role of boron in mechanical performance is dual. Low boron dosages (5–10%) promote BO_4 formation, generating a more compact gel network and improving compressive strength (Kaya et al.,

2023). However, at boron levels ≥15%, the dominance of BO_3 species, excessive ionic release due to rapid dissolution, and increased microporosity lead to a reduction in strength (Hajimohammadi et al., 2017). MgO addition mitigates this drawback by accelerating polycondensation kinetics through Mg^{2+} interactions and promoting the formation of dense B–Mg–Si–Al gel structures—an effect confirmed in multiple studies (Abdullah et al., 2022b).

Microstructural evaluations also support these trends. At low boron contents, homogeneous and dense gel regions are observed, while higher boron dosages yield discontinuous gel morphologies, increased porosity, and partially vitrified zones (Wang et al., 2020c). SEM analyses confirm that MgO reduces void structure and contributes to a more compact matrix (Kaya et al., 2023). XRD findings indicate the development of borosilicate phases at elevated temperatures, which significantly enhance structural stability.

Since boron modifies matrix density and porosity, it is a critical determinant of durability. Low boron levels (5–10%) produce a dense and continuous gel network, narrowing capillary pores and reducing water absorption—thus yielding improved resistance to chemical attack (He et al., 2025; Karlıoğlu-Kaya & Onur, 2021). In contrast, increasing boron content leads to BO_3-dominated irregular bonding and excessive ionic release, resulting in higher porosity, increased permeability, and greater vulnerability to acidic and saline environments (Wang et al., 2020c; Liu et al., 2024). Studies report that high boron levels cause notable strength degradation under sulfate, chloride, and acidic exposure. MgO addition promotes B–Mg–Si–Al hybrid gel formation, partially compensating for boron-induced microstructural weakness (Abdullah et al., 2022b).These performance differences are reflected in the comparative results summarized in Table 5.1.

Table 5.1. Effect of Boron Content on Geopolymer Properties

Performance Parameter	**Low Boron (5–10%)**	**High Boron (15%+)**	**Reference**
Setting behavior	Moderate delay	Very long delay	He et al. (2021)
Compressive strength	Increased; compact gel	Decreased; higher porosity	Hajimohammadi et al. (2017); Abdullah et al. (2022a)
Microstructure	Homogeneous, dense gel	Porous, irregular structure	Kaya et al. (2023)
Thermal behavior	High stability	Moderate stability	Kaya et al. (2023)
Water absorption	Low	High	Karlıoğlu-Kaya & Onur (2025)

The comparative results in Table 5.1 clearly illustrate that boron content produces a threshold effect on geopolymer performance. Low boron levels (5–10%) extend setting time moderately, enhance compressive strength, promote compact gel formation, and improve thermal stability and water absorption behavior. In contrast, high boron levels (15%+) result in increased porosity, pronounced setting delays, mechanical weakening, and reduced durability due to higher permeability. Overall, most studies indicate that the optimum boron range for durability and mechanical performance lies between 5% and 10%, providing the best balance between strength, permeability, and chemical stability.

6. Potential of Boron Waste–Incorporated Geopolymers

Boron waste–incorporated geopolymers are multifunctional inorganic binders that can be adapted for various high-performance engineering applications due to the chemical and microstructural

modifications induced by boron-containing phases during geopolymerization. The dissolution of borate species in alkaline media leads to the formation of BO_3 and, more importantly, BO_4 units, which partially convert the N–A–S–H gel network into B–A–S–H phases during polycondensation. This transformation increases bond density and enhances the viscoelastic stability of the matrix (Hajimohammadi et al., 2017; Wang et al., 2020). Such chemical restructuring within the geopolymer gels plays a decisive role in governing both mechanical and functional properties.

High-temperature performance is one of the prominent advantages of boron-modified geopolymers. Glassy borosilicate phases associated with the increased presence of BO_4 tetrahedra have been shown to form stably between 600 and 800 °C, effectively preserving the integrity of the matrix (Wang et al., 2020b; Abdullah et al., 2022a; Kaya et al., 2023). These phases limit crack formation under elevated temperatures, improve thermal shock resistance, and enhance dimensional stability. Therefore, boron-containing geopolymers represent strong candidate materials for refractory substrates, fire-resistant panels, thermal barrier coatings, and other structural components exposed to high temperatures.

Boron also contributes significantly to mechanical performance. Low to moderate boron contents (5–10%) promote the formation of dense B–O–Si linkages within the gel network, resulting in more compact microstructures and increased strength (He et al., 2025; Kaya et al., 2023). At higher boron levels, however, the dominance of BO_3 species promotes microvoid formation and leads to reductions in mechanical strength (Wang et al., 2020c). The addition of MgO produces a synergistic effect with boron by facilitating the formation of B–Mg–Si–Al hybrid gels, which markedly enhance mechanical stability (Abdullah et al., 2022b).

Microstructural refinement impacts not only mechanical behavior but also durability. Dense gel networks formed at optimum boron contents (5–10%) restrict capillary pores, reducing water absorption and enhancing resistance to chemical attack (Karlıoğlu-Kaya & Onur, 2025). At higher boron levels, increased porosity elevates chemical permeability and leads to performance degradation under acidic or saline conditions (Wang et al., 2020). These trends highlight the critical importance of boron concentration as a design parameter for engineering applications.

Beyond structural properties, boron provides functional advantages that position these materials uniquely in specialized applications. The high neutron capture cross-section of boron makes boron-modified geopolymers effective shielding materials for nuclear engineering uses (He et al., 2025). The B–O–Si networks within the matrix restrict the diffusion of radionuclide ions, providing the chemical stability required for radioactive waste immobilization (Liu et al., 2024). These properties make boron-containing geopolymers strong alternatives for reactor barrier systems, storage modules, and radiation protection infrastructures. The functional advantages across different application domains are summarized in Table 6.1.

Table 6.1. Functional Advantages of Boron Incorporation in Geopolymer Systems

Application Area	**Key Requirement**	**Advantage of Boron-Modified Geopolymers**	**Reference**
High-temperature applications	Thermal stability, glassy phase formation	Stable structure at 600–800 °C	Kaya et al. (2023)
Lightweight components	Low density, reduced thermal conductivity	Controlled micro-porosity	He et al. (2021); Wang et al. (2020c)

Radiation shielding	Neutron and gamma absorption	High neutron capture cross-section of boron	Kim et al. (2025)
Waste immobilization	Low permeability, chemical stability	Ion binding via B–O–Si networks	Liu et al. (2024)
Chemical resistance	Acid and sulfate durability	Compact matrix, low water absorption	Karlıoğlu-Kaya & Onur (2025)

The results summarized in Table 6.1 demonstrate that boron waste incorporation provides multidimensional enhancements in thermal stability, mechanical strength, chemical resistance, ion immobilization, and radiation shielding performance. The development of BO_4-based gel structures and glassy borosilicate phases renders boron-containing geopolymers suitable for high-temperature, chemically aggressive, and radiation-intensive environments. These findings indicate that boron waste should not be regarded merely as a recycled by-product but as a strategic chemical modifier that enhances the functional performance of geopolymer systems.

7. Conclusions and Future Perspectives

Findings on boron waste–incorporated geopolymers demonstrate that boron functions not merely as an additional component but as a multidimensional regulator that simultaneously influences dissolution kinetics, polycondensation mechanisms, and microstructural evolution. The BO_3/BO_4 transformations occurring in alkaline media directly determine the chemical composition and density of the gel phases, which in turn play decisive roles in mechanical strength, thermal stability, and chemical resistance (Hajimohammadi et al., 2017). At low boron levels, the dominance of BO_4 units enhances gel compactness and improves strength, whereas at high concentrations, the prevalence of BO_3-based linkages increases porosity and leads to performance losses (Wang et al., 2020c). The synergistic interaction between boron and MgO promotes the formation of dense B–Mg–Si–Al gel phases, further enhancing both mechanical behavior and high-temperature performance (Abdullah et al., 2022b). The structural and performance implications of boron-induced chemical processes are summarized analytically in Table 7.1.

Table 7.1. Summary of Boron–Geopolymer Interactions

Boron-Induced Effect	**Microstructural Outcome**	**Macroscopic Effect**	**Reference**
BO_4^- formation	Increased bond density	High strength, low porosity	Kaya et al. (2023)
BO_3 dominance	Irregular gel, weak bonding	Strength loss, increased water uptake	Wang et al. (2020c)
Boron–MgO interaction	Hybrid B–Mg–Si–Al gels	Enhanced mechanical & thermal performance	Abdullah et al. (2022b)
Glassy borosilicate phase	Pore closure	High-temperature resistance	Kaya et al. (2023)
Neutron absorption	BO_3/BO_4 core effects	Radiation-shielding capability	Kim et al. (2025)
Controlled boron dissolution	Compact gel zones	Optimum density for lightweight components	He et al. (2021)

The results presented in Table 7.1 indicate that the effects of boron in geopolymer systems are highly sensitive to its concentration and that performance varies directly with dosage. At low boron contents (5–10%), the dominance of BO_4 units increases gel density, reduces porosity, and improves both mechanical performance and chemical stability. At higher boron levels, however, the formation of BO_3-based irregular networks accelerates void development, leading to strength reductions and increased permeability. MgO addition partially compensates for these drawbacks by promoting the development of dense B–Mg–Si–Al gels. Overall, the optimum boron content in geopolymers is typically within the 5–10% range, which provides the best balance of strength, permeability, and chemical durability. Furthermore, considering their low permeability, high chemical stability, and the strong neutron-capture capability of boron, boron-containing geopolymers offer unique advantages for applications requiring radiation shielding, waste immobilization, and elevated-temperature performance.

Despite the broad potential of boron waste in geopolymer production, variability in chemical composition and dissolution behavior presents challenges for achieving industrial-scale consistency. Therefore, future research should prioritize three main areas:

1. Atomic-scale modeling of BO_3/BO_4 transformations

– Molecular-level understanding of reaction mechanisms (MD, DFT).

2. Standardization of industrial boron wastes

– Development of unified characterization protocols (XRF, XRD, TGA).

3. Long-term durability and environmental performance

– Leaching behavior, phase stability, fatigue resistance, chemical-attack durability.

Additional promising directions include applications in nuclear engineering, ceramic–geopolymer hybrid systems, low-density thermal panels, functional barrier materials, and multivariable optimization using Taguchi, ANN, and GA algorithms.

In conclusion, boron waste is not merely a recovered by-product but a strategic component that enhances the chemical and physical performance of geopolymers in multiple dimensions. Its integration into sustainable binder technologies supports circular economy goals and provides significant potential for advanced engineering applications. Interdisciplinary future studies will accelerate the adoption of boron-containing geopolymers as a reliable and high-performance material class at the industrial scale.

Referances

Abdullah, M. M. A. B., Ismail, K., & Rahman, R. A. (2022a). Influence of MgO on alkali-activated materials: Reaction mechanism and mechanical properties. Construction and Building Materials, 318, 125–133.

Abdullah, M. M. A. B., Yong, H. C., Zamri, N. A., & Abd Razak, R. A. (2022b). Influence of MgO and boron-containing additives on geopolymerization. Construction and Building Materials, 329, 127105.

Alkan, M., Doğan, M., & Turhan, Y. (2017). Characterization of boron industry wastes and their potential use in construction materials. Waste Management, 67, 150–160.

Aydın, S., & Kızıltepe, C. Ç. (2019). Valorization of boron mine tailings in alkali-activated mortars. Journal of Materials in Civil Engineering, 31(10), 04019224.

Benk, A., Öztaş, A., & Yılmaz, G. (2013). Recycling possibilities of boron waste in building materials. Construction and Building Materials, 40, 223–229.

Bernal, S. A., Provis, J. L., Brice, D. G., Kilcullen, A. R., Duxson, P., & van Deventer, J. S. J. (2014). Accelerated carbonation testing of alkali-activated binders. Cement and Concrete Research, 57, 33–43.

Davidovits, J. (2020). Geopolymer chemistry and applications (5th ed.). Geopolymer Institute.

Gür, T., Acar, İ., & Yalçın, B. (2020). Assessment of boron waste materials for industrial applications. Journal of Environmental Chemical Engineering, 8(5), 104–112.

Hajimohammadi, A., Provis, J. L., & van Deventer, J. S. J. (2017). Effect of boron on geopolymerization. Cement and Concrete Research, 99, 10–19.

He, M., Li, N., Ou, Z., Huang, Y., Qu, F., Unluer, C., & Yang, Z. (2025). Effect of borax and magnesia on setting, strength, and microstructure of acid-activated fly ash geopolymers. Construction and Building Materials, 498, 144013.

Hussein, M., Ibrahim, M., & Rashad, A. (2021). Review on the sustainable development of alkali-activated materials using waste-derived activators: Mechanical and environmental perspectives. Construction and Building Materials, 270, 121–150.

Karahan, S., & Yıldız, E. (2022). Characterizing boron-enhanced one-part alkaline-activated mortars: Mechanical, microstructural and thermal performance. Construction and Building Materials, 345, 128–142.

Karlıoğlu-Kaya, A., & Onur, M. İ. (2025). Optimization of physical, mechanical and thermal properties of two-part geopolymer mortar by Taguchi method. Construction and Building Materials, 476, 141208.

Kaya, M., & Demir, İ. (2022). Development of one-part geopolymer binder produced from alkali-fused boron mine tailings. Ceramics International, 48(12), 18132–18145.

Kaya, M., Ersöz, M., & Uzun, B. (2023). Thermal behavior and microstructural evolution of boron-modified geopolymer composites. Ceramics International, 49(1), 1234–1246.

Kızıltepe, C. Ç., Yüksel, İ., & Aydın, S. (2025). Development of one-part geopolymer binder produced from alkali-fused boron mine tailings. Journal of Building Engineering, 111, 113099.

Kim, M., Lee, S., Kim, G., Park, S., & Lee, B. (2025). A novel borated cementitious material for neutron and gamma-ray shielding. Construction and Building Materials, 479, 141444.

Liu, J., Xu, Y., Zhang, W., Ye, J., & Wang, R. (2024). Solidification performance and mechanism of typical radioactive nuclear waste by geopolymers and geopolymer ceramics: A review. Progress in Nuclear Energy, 169, 105106.

Provis, J. L. (2018). Alkali-activated materials. Cement and Concrete Research, 114, 40–48.

Scrivener, K. L., John, V. M., & Gartner, E. M. (2018). Eco-efficient cements: Potential economically viable solutions for a low-CO_2 cement-based materials industry. Cement and Concrete Research, 114, 2–26.

Serdar, M., & Cavit, A. (2019). Mechanical and microstructural performance of alkali-activated waste clay containing boron. Construction and Building Materials, 225, 1042–1053.

Tayibi, H., Choura, M., López, F. A., Alguacil, F. J., & López-Delgado, A. (2009). Environmental impact and management of phosphogypsum. Journal of Environmental Management, 90(8), 2377–2386.

Wang, J., Liu, S., & Xu, H. (2020a). Selected performance of alkali-activated mine tailings as cementitious composites: A review. Journal of Materials Research and Technology, 9(5), 11830–11848.

Wang, L., Zhang, Y., & Sun, H. (2020b). Network structure modification in boron-containing geopolymer gels. Journal of Non-Crystalline Solids, 543, 120137.

Wang, Y., Li, X., & Sun, Z. (2020c). Role of boron in the microstructure development of alkali-activated binders. Journal of Non-Crystalline Solids, 543, 120128.

Zhang, L., Li, Y., & Chen, X. (2023). Advancements in the properties of industrial solid waste-based cementitious materials: A review. Journal of Cleaner Production, 412, 137004.

Chapter 4

FRICTION AND WEAR BEHAVIOR OF PACK-BORIDED CO-BASED SUPERALLOY

Melik ÇETİN[1], Kenza DJEBARI[2], Ali GÜNDOĞAR[3]

1 Prof.Dr.Melik ÇETİN, Karabuk University, Engineering and Natural Sciences Faculty, Department of Metallurgy and Materials Engineering, ORCID: 0000-0002-6952-2523
2 Dr. Kenza DJEBARI, Karabuk University, Engineering and Natural Sciences Faculty, Department of Metallurgy and Materials Engineering, ORCID: 0000-0003-0158-4741
3 Ali GÜNDOĞAR, Yapı Kredi Bankası A.Ş. Genel Müdürlüğü, Beşiktaş İstanbul, ORCID: 0009-0006-5986-3515

Introduction

Cobalt-based superalloys are high-temperature materials that exhibit a good combination of strength and corrosion resistance (Coutsouradis et al., 1987; Sato et al., 2006). In addition, due to their outstanding oxidation resistance and stress-rupture properties, they are a class of superalloys that can be used in applications such as nuclear reactors and in the aerospace industry for the manufacturing of gas turbine combustion chambers or turbine blades (Yang et al., 2019; Motallebzadeh et al., 2015; Du et al., 2018; Vashishtha et al., 2018; Mapelli et al., 2020; Ahmed et al., 2021). These alloys are designed to provide high-temperature strength by combining solid-solution and carbide strengthening (Coutsouradis et al., 1987; Sato et al., 2006; Mapelli et al., 2020). With technological advancements, the addition of new alloying elements, and the development of modern coating techniques, the oxidation, wear, and corrosion resistance of cobalt-based alloys have improved. Progress in the physical metallurgy of Co-based alloys has enabled them to endure greater mechanical stresses at elevated service temperatures (Mapelli et al., 2020). Unlike other alloy systems, particle strengthening does not play a significant role in increasing the strength of cobalt-based superalloys; instead, strengthening mechanisms are achieved through solid-solution hardening and carbide formation (Ahmed et al., 2021; Campos et al., 2014; Wang et al., 2020; Costa et al., 2022). Carbides precipitate along grain boundaries and dendritic regions, thereby enhancing the material's strength. Secondary carbides precipitate at elevated temperatures, impede dislocation motion, prevent grain-boundary sliding, and increase strength (Coutsouradis et al., 1987; Sato et al., 2006). Despite the exceptional performance of these alloys, wear-related problems are frequently observed. Recently, thermochemical treatments applied to material surfaces have attracted considerable interest, as they have been used to eliminate potential surface-related issues and have provided significant improvements in wear resistance (Campos et al., 2014; Cuao-Moreu et al., 2019; Campos-Silva et al., 2019; Campos et al., 2019; Wang et al., 2018). However, rapid solidification during coating deposition can lead to residual stresses when splats impact the substrate, resulting in microcrack formation within the coating (Wang et al., 2018). Therefore, eliminating coating defects and residual stresses is a key concern, and improving the strength and toughness of thermally sprayed alloy coatings has received widespread interest. Additionally, it is well established that heat treatment can effectively improve the mechanical, wear, and corrosion properties of coatings (Liu et al., 2018; Hao et al., 2018; Safavi & Rasooli, 2019; Chen et al., 2018). In Co-based coatings, heat treatment has been reported to enhance cavitation-erosion resistance via atomic diffusion significantly (Wang et al., 2016). Although these alloys are widely used in advanced engineering applications and exhibit higher surface hardness than Ni-based superalloys, their performance remains insufficient for abrasive environments. Therefore, studies have been conducted to improve the surface hardness of cobalt-based superalloys using thermochemical methods (Mapelli et al., 2020; Ahmed et al., 2021; Campos et al., 2014; Wang et al., 2020; Costa et al., 2022). Examination of the literature shows that most research among cobalt-based alloys has been carried out on the CoCrMo system (Campos-Silva et al., 2014; Cuao-Moreu et al., 2019; Campos et al., 2019; Mu & Shen, 2010; Campos-Silva et al., 2013), whereas studies on the Haynes 25 alloy remain limited (Girişken & Güral, 2023; Günen & Ergin, 2023). As with other superalloys, cobalt-based grades used in industry can generally be categorized into two groups: cast alloys such as X40 and MAR-M-302 and wrought alloys, including Haynes 25, Haynes 188, and S-816 (Gialanella & Malandruccolo, 2020; De Faria Cunha et al., 2023).Surface hardening processes are commonly employed to enhance the resistance of many material groups in abrasive environments. Surface hardening may be achieved through heat treatment and quenching, or by diffusion of one or more elements to form deposited layers on the material surface (Campos & Rodriguez-Castro, 2015; Kulka, 2019). Diffusion-based techniques used to improve surface properties typically rely on diffusing small atoms to form an interstitial solid solution, followed by chemical reactions between the deposited atoms and the base metal to produce surface compounds (Campos & Rodriguez-Castro, 2015). Among current industrial surface hardening and performance-enhancement applications, methods like carburizing, nitriding, carbo-nitriding, nitro-carburizing, boriding, physical vapor deposition, and chemical vapor deposition are

widely used. Among these processes, boriding is more commonly preferred because it imparts high surface hardness (Kulka, 2019; Günen & Kanca, 2017). Boriding is a surface hardening method in which boron, characterized by a small atomic radius, is diffused into metallic materials at temperatures between 700 and 1050°C for 1 to 12 hours, resulting in boride layers of specific thickness depending on processing time (Kulka, 2019; Gunes, 2013). The resulting boride layer exhibits high hardness, a low friction coefficient, and improved corrosion resistance under acidic and basic corrosive conditions and at elevated temperatures. Thus, boriding enhances tribological performance and corrosion resistance by forming a boride layer on the surface (Gunes, 2022; Günen et al., 2018). The most widely used boriding technique is pack boriding because it is cost-effective, easy to apply, and more environmentally friendly (Keddam & Chentouf, 2005; Gunen et al., 2022). In their study, Girişken and Güral (2023) applied boriding at 850°C, 950°C, and 1050°C for 4 h to the Haynes 25 Co-based superalloy. They reported that borided specimens exhibited high wear resistance under ambient conditions and 500°C, with abrasive, oxidative, and plastic deformation mechanisms identified, and an oxidative and fracture mechanism identified, respectively. In another study, Günen and Ergin (2023) borided Haynes 25 at 950°C for 3 h, obtaining a boride layer thickness of 37.58 ± 2.85 μm and a hardness of 26.34 ± 2.33 GPa, confirming an increase in hardness.

Studies in the literature show that research involving Co-based superalloys has been conducted almost exclusively on CoCrMo alloys (Campos et al., 2014; Cuao-Moreu et al., 2019; Campos-Silva et al., 2019; Mu & Shen, 2010; Campos et al., 2013), while studies performed on the Haynes 25 superalloy are insufficient (Girişken & Güral, 2023; Günen & Ergin, 2023). Furthermore, no studies have been reported on the wear and friction behavior of borided samples under different cooling media or cooling conditions after boriding. In this study, the boriding of the cobalt-based Haynes 25 superalloy by a thermochemical method, the cooling of the borided specimens in three media (furnace, air, and water), the determination of microhardness values, and the investigation of wear behavior at 350°C were emphasized. SEM, XRD, and microhardness analyses were performed to investigate both the boride layers and the wear surfaces
.

2. Materials and Methods

The substrate employed in this investigation was the Haynes 25 Co superalloy (commonly referred to as L605). This alloy is primarily composed of cobalt, with notable additions of nickel, chromium, and tungsten. Based on the manufacturer's specifications, its composition includes approximately 10% Ni, 20% Cr, 15% W, 3% Fe, 1.5% Mn, 0.4% Si, and 0.1% C, with cobalt constituting the remainder (Kramer et al., 1998).

2.1. Processing Route for Thermochemical Coatings

Twenty-five Haynes 25 specimens measuring 30 × 30 × 4 mm^3 were sectioned using a precision cutting saw. Before the boriding treatment, the sample surfaces were prepared by sequential grinding with 400–1000 grit SiC abrasive papers, followed by rinsing under running water and drying with ethyl alcohol to eliminate residual contaminants. The boriding mixture consisted of 90% B_4C (boron carbide) and 10% $NaBF_4$ (sodium tetrafluoroborate). Boriding was performed at 975 °C for 5 h under controlled atmospheric conditions (Kramer et al., 1998; Gündoğar, 2024; Metals Handbook, 1983). During processing, the specimens were embedded in the boriding agent inside threaded AISI 321 stainless-steel crucibles, ensuring a minimum powder packing depth of 10 mm. Finely ground SiC

(commercial Ekrit powders) was added on top to minimize oxygen penetration and prevent oxidation at elevated temperatures. The crucibles were sealed and loaded into the furnace for diffusion-based boriding. Following boriding, the samples were cooled under three different conditions: furnace cooling, open-air cooling, and water quenching.

2.2. Characterization

The coated specimens were sectioned into 15 × 15 × 4 mm^3 pieces to prepare both metallographic and XRD samples. Prior to microstructural examination, the surfaces were ground and polished according to standard procedures, followed by etching in a 1:3 HNO_3/HCl solution to reveal microstructural features. Vickers microhardness tests were performed under a 100 gf load with a 15 s dwell time, starting at the coating surface and progressing toward the substrate at 10 μm intervals. Depending on the coating type, fracture toughness was assessed using loads of either 300 gf or 500 gf for 15 s. To assess the nanoscale mechanical behavior of the coatings and to determine their elastic modulus, nanoindentation measurements were performed with a 10 μN load and a 15-second dwell time. The microstructures of the coated layers were examined using a Nikon MA100 optical microscope and a Thermo Fisher Scientific Apreo S scanning electron microscope. Phase identification was performed using a Malvern Panalytical EMPYREAN X-ray diffractometer with Cu-Kα radiation (λ = 1.540598 Å) and a 1 ° step size, scanning from 20 ° to 90 °. Wear behavior was assessed on a TURKYUS ball-on-disk apparatus at 25 °C, 350 °C, and 600 °C under dry sliding conditions. Tests were performed with a sliding velocity of 375 mm/s for 667 s, using a 20 N load and a total sliding distance of 250 m against a 6-mm-diameter Al_2O_3 ball (hardness: 1650 MPa). The depth and width of the wear tracks were measured using a 2D profilometer, and the obtained dimensions were used to calculate wear rates in accordance with previously established methodologies (Günen & Kanca, 2025; Ahlatçı et al., 2025; Deng et al., 2025). Subsequently, SEM and EDS analyses of the worn regions were performed to determine the prevailing wear mechanisms.

3. Characterization Results and Discussion

At a constant temperature of 975 °C, the microstructural images of the Haynes 25 superalloy borided for 5 hours and left unprocessed, obtained using Scanning Electron Microscopy (SEM) and line EDAX, are illustrated in Figure 1, respectively, for the untreated sample and the borided samples cooled in furnace, air, and water environments. Figure 1 presents the SEM images of the untreated sample. Upon examination, numerous small white spots are observed on the surface of the Haynes 25 superalloy. These structures can be interpreted as reflecting the sample's microstructural

components, impurities, and surface defects. The black pits observed at a distance from one another can be interpreted as regions where precipitates are located. It can also be stated that similar appearances may occur in phase segregations.

When the EDAX analysis is evaluated, it is seen that the distribution of three different elements is present. These elements are the main constituents of the superalloy, and their presence is dominant over that of the other elements. When we examine the graphs from top to bottom, the CoKα1 graph shows the distribution of cobalt. The graph indicates that cobalt is homogeneously distributed along the surface. The NiKα1 graph shows the distribution of nickel. Based on the graph, nickel also exhibits a homogeneous distribution across the surface. From the WKα1 graph, we can conclude that the tungsten distribution is more fluctuating than those of Co and Ni. Although it exhibits strong diffraction, it still shows a certain level of homogeneity. These analyses indicate that the elements on the material's surface are uniformly distributed and confirm that no subsequent coating or processing was applied to the surface (untreated sample).

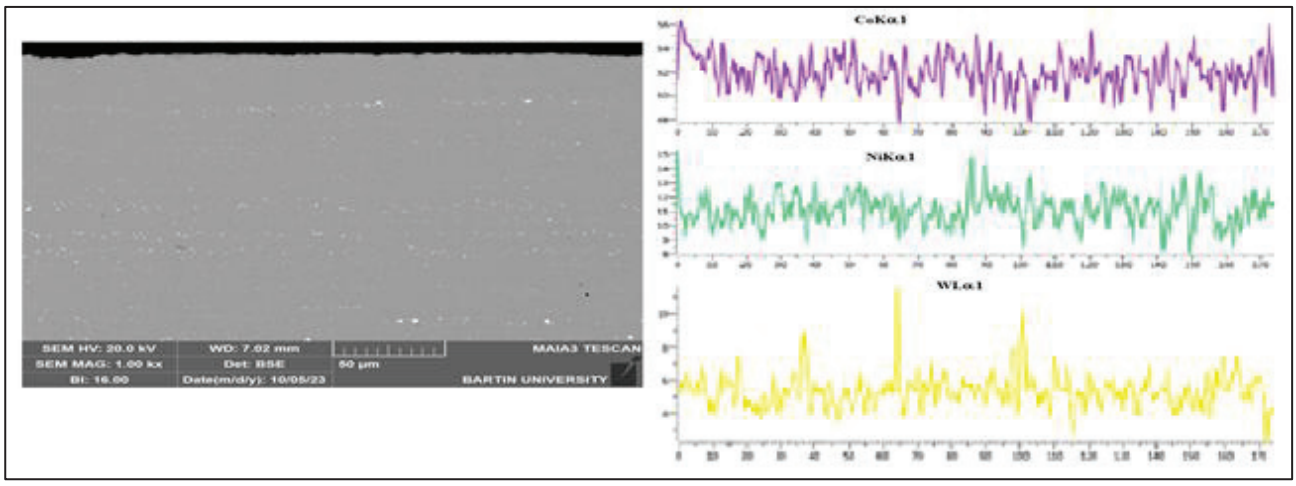

Figure 1. SEM line EDAX images and values of the untreated sample.

In Figure 2(a-d), the cross-sectional images showing the boride layer thicknesses of the untreated Haynes 25 sample and the samples borided at 975 °C for 5 hours and subsequently cooled in a furnace and in air are presented. In the images shown in Figure 2, (a) represents the untreated sample, while (b–c) represent the borided samples. The boriding process was performed at a constant temperature of 975 °C for 5 hours, and the boride layer thicknesses obtained upon cooling in different environments are given. The surface thickness measurements of the untreated sample, shown in Figure 2(a), are 5.44 µm, 4.06 µm, 5.28 µm, and 8.03 µm. In Figure 2(b), when the boride layer depth of the furnace-cooled sample is measured in the cross-sectional microstructure, it is determined to be 54.50 µm, 48.14 µm, 56.31 µm, 64.36 µm, 37.55 µm, and 46.70 µm, respectively. The boride layer thicknesses of the air-cooled sample shown in Figure 2(c) were measured as 23.12 µm, 33.32 µm,

31.25 µm, 41.24 µm, 20.32 µm, and 24.37 µm, respectively. In Figure 2(d), the boride layer depth for the specimen cooled in water is measured in the cross-sectional microstructure and found to be 54.50 µm, 48.14 µm, 56.31 µm, 64.36 µm, 37.55 µm, and 46.70 µm, respectively.

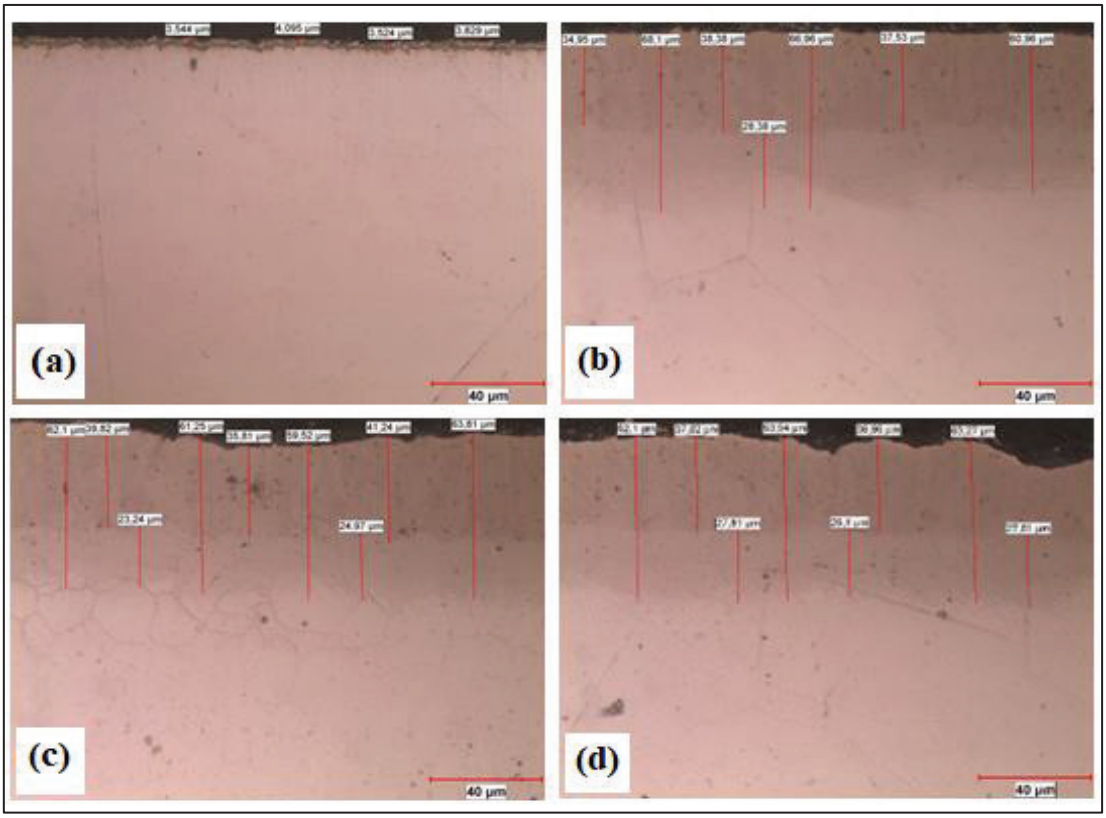

Figure 2. Cross-sectional images illustrating the boride layer thicknesses of Haynes 25 samples subjected to boriding at 975 °C for 5 hours, including: (a) the unprocessed sample, (b) the sample subjected to furnace cooling, (c) the sample cooled in ambient air, and (d) the sample cooled in water.

Figure 3 illustrates the change in microhardness from the surface toward the matrix for the untreated Haynes 25 alloy, the specimen borided at 975 °C for 5 hours, and the borided samples subjected to furnace, air, and water cooling. As depicted in the figure, the hardness gradually declines with increasing depth. This reduction is attributed to the limited inward diffusion of boron atoms. The drop in hardness becomes more significant at the interface between the boride layer and the diffusion zone, whereas the matrix shows a more uniform and nearly linear decrease with minimal fluctuation. The peak hardness values are located within the boride layer, primarily because of the presence of Cr-B and W-B phases. These phases typically reach hardness levels of about 30 GPa, while other potential borides, including Ni-B (9–16 GPa), Co-B (16–18 GPa), and Fe-B (16–20 GPa), display comparatively lower hardness. Among the untreated, furnace-cooled, and air-cooled specimens, the highest hardness was recorded for the sample borided at 975 °C for 5 hours and cooled in air. Furthermore, as shown in Figure 3, the water-cooled specimen contains a greater proportion of harder

phases, such as Cr-B and Co-W-B, than the Co-B phase. The untreated Haynes 25 alloy shows a microhardness of approximately 566 HV0.025, whereas boriding increased it to 1619–1971 HV0.025. Through bording, the boriding treatment enhanced the surface hardness of Haynes 25 by approximately 4.38-fold.

The graph shows the variation in microhardness (HV0.025) with depth from the surface for the four conditions (untreated, thermally treated via furnace, air, and water cooling). The influence of each cooling process on the microhardness of the tested samples can be explained as follows: the untreated sample shown in the graph has a microhardness of approximately 500 HV and shows slight variation with increasing depth from the surface.

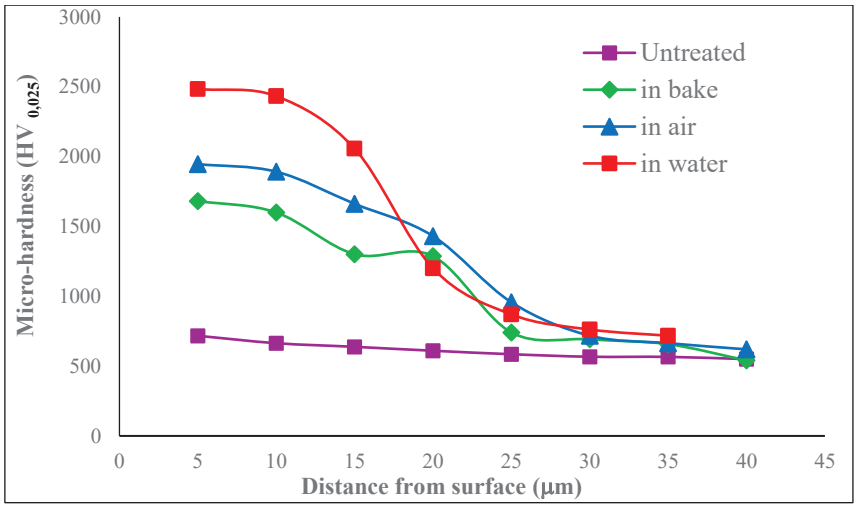

Figure 3. Hardness profiles for the untreated and borided Haynes 25 samples cooled in different cool environments.

The low, nearly constant microhardness values observed for the untreated sample indicate that boriding did not produce a substantial increase in surface hardness and that the resulting boride layer is nonuniform. The gradual reduction in hardness from the surface toward the substrate can be attributed to the limited inward diffusion of boron. Although a marked decline in hardness is evident between the coating and the diffusion zone, the minimal variation within the matrix suggests that this region remains largely unaffected by the heat treatment and preserves its original microstructural characteristics. The maximum hardness is observed within the boride layer, attributed to the formation of high-hardness phases such as Cr-B and W-B, embedded among Co-B and Co_2B phases (Metals Handbook, 1983; Deng et al., 2015; Campos-Silva et al., 2019). When the values of the furnace-cooled sample are examined, it is seen that the microhardness begins at approximately 2500 HV at the coating surface (sample surface), rapidly decreases after 20 µm, and falls to about 700 HV at a depth of 40 µm. Because furnace cooling provides controlled cooling, the resulting boride layer is thick and hard. The effective penetration of boron atoms into the surface indicates that the boriding

process was effective. The microhardness of the air-cooled sample increases to approximately 2000 HV at the surface, then decreases beyond a depth of 15 μm, falling to about 500 HV at 40 μm. Compared to furnace cooling, air cooling results in a thinner boride layer due to less controlled cooling conditions. However, the surface hardness is significantly higher than that of the untreated sample, indicating that the boriding process improves surface properties. The microhardness of the water-cooled sample is approximately 2400 HV at the surface and rapidly decreases beyond 15 μm, reaching around 500 HV at 40 μm. Water cooling contributes to achieving a homogeneous, effective boride layer by providing high surface hardness. This indicates that rapid cooling after boriding helps retain surface hardness. The results show that boron atoms penetrate the surface more effectively. In summary, the results in Figure 3 show that different cooling treatments have significant effects on the microhardness of the borided samples. Furnace cooling provides the highest and most homogeneous hardness distribution, while water cooling similarly enables high surface hardness. Air cooling results in lower, yet still high, hardness values, whereas the untreated sample exhibits the lowest hardness.

Figure 4 presents the wear test outcomes at 350 °C for the Haynes 25 specimens. As shown in the results, the untreated alloy exhibited the highest wear rate, whereas the sample cooled in water exhibited the lowest. The wear behavior of the air-cooled and furnace-cooled specimens is nearly comparable. Moreover, the measurements indicate an inverse correlation between wear rate and wear scar depth. Across all cooling conditions, the borided samples showed markedly improved wear resistance compared with the untreated alloy. The elevated wear rate of the uncoated specimen is attributed to the lack of a protective boride layer, which leaves the surface more susceptible to abrasive wear. In contrast, the furnace-cooled sample showed a lower wear rate, indicating that the boride layer formation enhances surface durability and protects the material against wear. Similarly, the air-cooled sample exhibited a wear rate close to that of the furnace-cooled specimen.

This shows that both cooling methods provide similar protective effects and that the layer formed after boriding increases wear resistance. The water-cooled sample has the lowest wear rate. This result suggests that cooling in water most effectively preserves the boride layer formed after boriding and maximizes wear resistance.

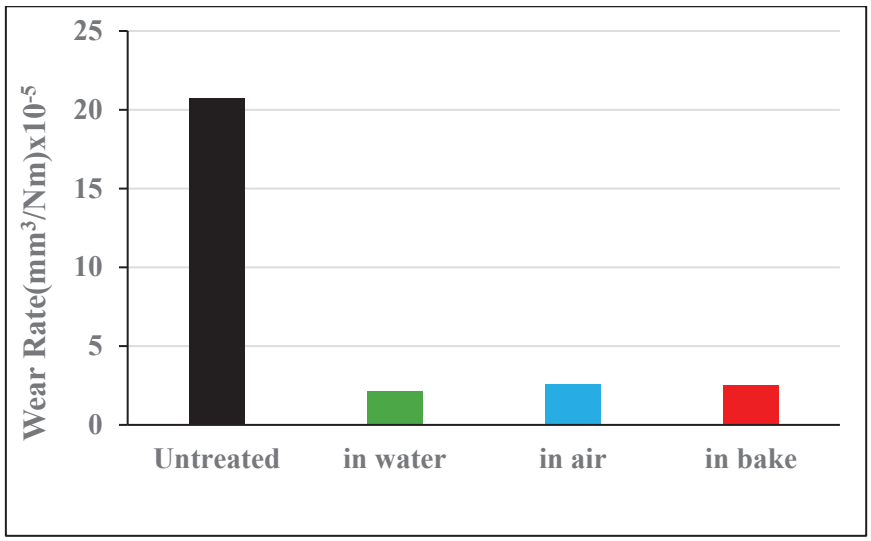

Figure 4. Wear rate values of Haynes 25 samples subjected to wear testing at 350 °C.

SEM micrographs of the worn surfaces of the untreated, furnace-cooled, and air-cooled samples abraded at 350 °C are presented in Figure 5. In Figure 5(a), the SEM micrograph of the untreated Haynes 25 sample abraded at 350 °C is shown. In this image, a distinct layered structure and cracks are visible on the surface. This indicates the mechanical stresses developed on the surface during abrasion and the subsequent fracture. The separations and cracks between the layers indicate that material was removed from the surface during abrasion. This situation suggests that thermal shock effects formed on the surface due to abrasion at high temperatures. Traces of plastic deformation were observed in some surface regions. These traces are formed by the softening of the material at elevated temperatures and by shape change under abrasive forces. Plastic deformation reduced wear resistance and increased surface material loss. In the images, free particles and debris are observed on the surface. These particles can be considered as fragments detached from the surface during abrasion. These detachments are one of the factors affecting the wear rate, and continue throughout the process. The detached particles also increased surface roughness. The high-temperature abrasion process on the untreated sample made thermal effects more pronounced on the surface. These thermal effects disrupted the material's structural integrity, accelerating wear. In Figure 5(b), the bright and large regions are thought to represent carbide phases. These phases are clearly and homogeneously distributed. Furnace cooling contributed to the homogeneous distribution of carbides, which enhances the material's hardness and wear resistance. The grain boundaries are highly distinct and regular, indicating that the grains have grown and become more pronounced. After abrasion, precipitation at grain boundaries is observed. This condition will increase the material's strength. The microstructure appears generally homogeneous. The uniform distribution of carbide phases indicates reduced surface roughness and improved mechanical properties. Furnace cooling, being a controlled cooling process,

reduces internal stresses and ensures a more balanced structure. The grain growth is homogeneous, the grain boundaries are distinct, and the precipitates appear uniformly distributed.

In Figure 5(c), the SEM images show that air cooling, being faster than furnace cooling, led to a more irregular and widespread distribution of carbide phases. The bright, large areas in the microstructure correspond to clearly visible carbide phases. SEM observations revealed the presence of three distinct zones in all borided specimens: the surface coating layer (boride layer), the diffusion or transition zone, and the underlying matrix. These regions are clearly distinguishable from one another. The SEM micrographs show that boriding produces a well-defined boride layer at the surface, which advances uniformly along the cross-section. This layer exhibits a relatively homogeneous and planar morphology. The intermediate region separating the boride layer from the matrix corresponds to the diffusion (transition) zone, a designation commonly found in the literature.

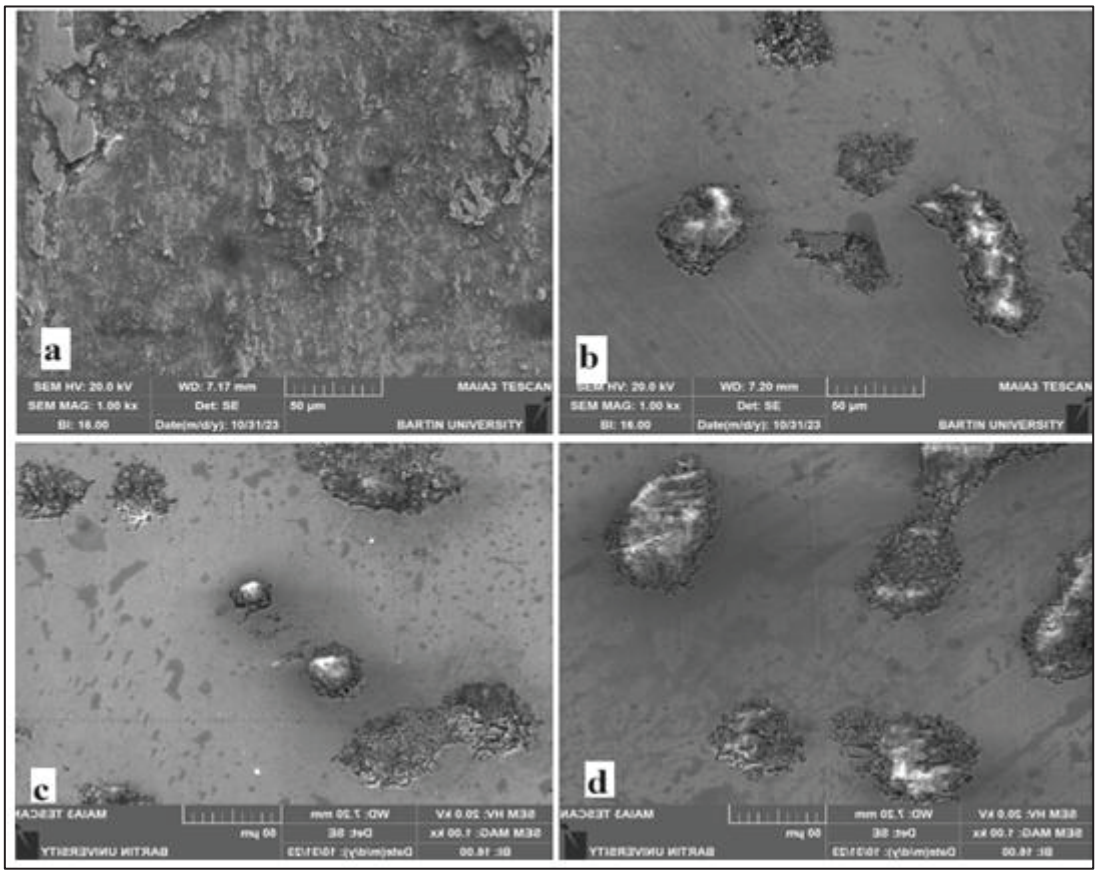

Figure 5. SEM micrographs illustrating the worn surfaces of the samples abraded at 350 °C: (a) the untreated specimen, (b) the specimen subjected to furnace cooling, (c) the air-cooled specimen, and (d) the water-quenched specimen.

This region appears significantly different from the metal treated. Although in many studies the borided portion (coating region) forms a thinner layer than the transition zone, in superalloys a thicker boride region than the transition zone has been observed after the boriding process (Günen et al., 2017). A similar observation is valid in this study. The transition zone is thinner compared to the

coating region. Since superalloys contain many elements in their structure, these elements reduce the diffusion rate of boron atoms and limit their movement toward the matrix region. Because the boride layer in Haynes 25 and other superalloys forms with relatively lower thickness, the thickness of the transition zones is also smaller. Many studies have concluded that transition zones have important benefits. The most important of these is providing a bridge between the coating and the substrate to accommodate the thermal expansion coefficients that develop during heating and cooling. Another important benefit is the increase in adhesion force between the substrate and the coating layer. In samples subjected to abrasion at 350 °C, the previously formed boride layer is significantly thinner than those produced by boriding at other temperatures and in different environments. The resulting thickness is 9.1 μm and 15.8 μm at the corners. As previously noted, a homogeneous, flat layer is obtained with no undesired impurities or surface defects, such as porosity. When the same treatment is applied, thicker layers can be obtained. Since the boriding process involves diffusion, a linear orientation and distinct regions are formed. Surface defects were not encountered during the treatments. The thickness of the boride layer, matrix, and transition regions increased. EDS examinations of the samples subjected to abrasion at 350 °C were carried out over a thickness of 100 μm. The analyses were performed on the sample surfaces, and it was determined that the grains had an orderly structure. Localized precipitates were observed. No tearing, cracking, or other anomalies were detected. The mapping image of the sample tested and abraded at 350 °C is presented in Figure 6. In Figure 6, the condition of the sample under the EDS microscope after abrasion at 350 °C is shown. Precipitates occurred in certain regions. The matrix, boride layer, and transition region were found to be layered. Elemental mapping of the relevant sample is also given in Figure 6. Figure 6 shows the mapping images of the elements present in the Haynes 25 superalloy. The precipitates formed in the coating after boriding were visualized. No anomalies such as tearing, porosity, or cracking were encountered. In the examined sample, the elements W, Mn, O, Co, Cr, and Ni were observed in considerable amounts in the structure after boriding. All these elements are present in the boride layer in varying proportions. The appearance of the layer formed for each element is very similar. The precipitates in the boride layer are also similar to one another. The Ni content in the boride layer is lower than that of the other elements. From the layer toward the matrix, the boron content decreases while the cobalt content increases. The SEM-EDS mapping image detected at 350 °C is shown in Figure 6. When the microstructures of the elements given in Figure 6 are examined, it is seen that Nb and B are present only in trace amounts in the samples abraded at 350 °C, and they do not significantly influence the layer. Fe and S are present in minimal amounts in the layer, whereas Al is present in greater amounts. However, even at these levels, Al separates from the other elements shown in Figure 6 and, based on findings over a 100 μm thickness, has a minimal effect on the characteristic structure of the boride layer. In addition, boron is concentrated around the layer. As the

movement progresses from the layer toward the matrix, the boron content decreases. In relation to this decrease, the cobalt content increases steadily toward the matrix and reaches high levels. The analyses show that, as in the untreated sample, cobalt is present in high amounts to maintain balance.

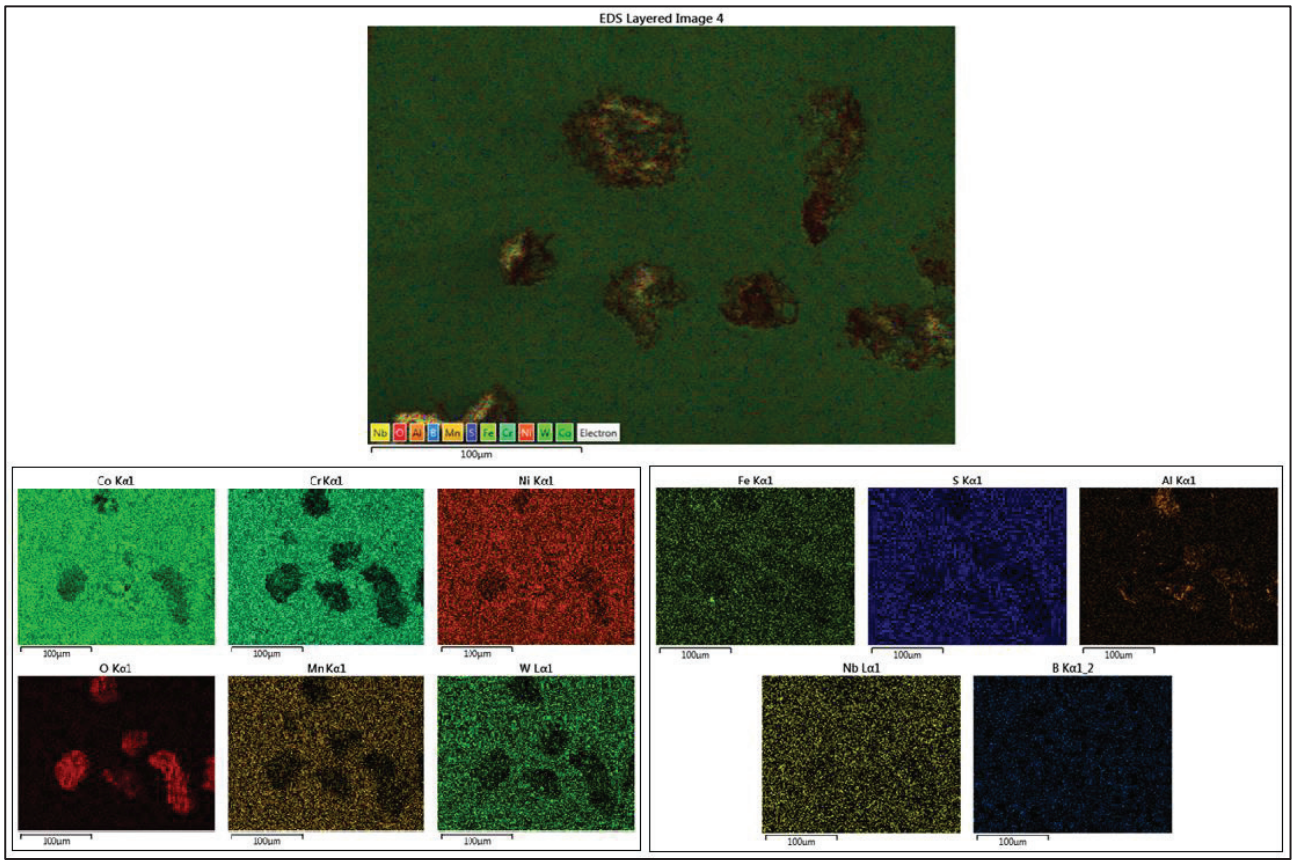

Figure 6. SEM-EDS elemental mapping of the sample abraded at 350 °C.

As seen in Figure 7, the amounts of Co, O, Cr, Ni, and W are high and dominant in the region, whereas S, Mn, B, and Nb are present in minimal quantities, and B and Nb were not detected at all. In the corresponding cross-sectional image, gray, black, and white colors were observed due to the influence of different alloying elements. It is understood that the observed deviations in the hardness test results are due to this condition in the region. The hardness readings of the Cr–B and W–B phases are around 20 GPa at 350 °C and approximately 25 GPa at 600 °C. The hardness of the other phases is significantly lower than these values. Compared with the gray region, the proportions of elements, except W, were similar in the white and black areasThe SEM microstructural findings align well with previously reported literature, indicating that the thickness of the boride layer increases as the treatment temperature rises. Alongside the boride layer growth, a corresponding thickening of the transition (diffusion) zone was also observed at higher temperatures, whereas a comparatively thinner transition region formed at 350 °C. Increasing the boriding temperature and extending the treatment

duration promote greater diffusion of boron atoms toward the surface. As a result, boron enrichment near the surface drives other alloying elements toward the transition zone. This behaviour reflects the combined influence of boriding temperature and exposure time on diffusion layer development (Doñu-Ruiz et al., 2021; Mu & Shen, 2010; Öge et al., 2023).

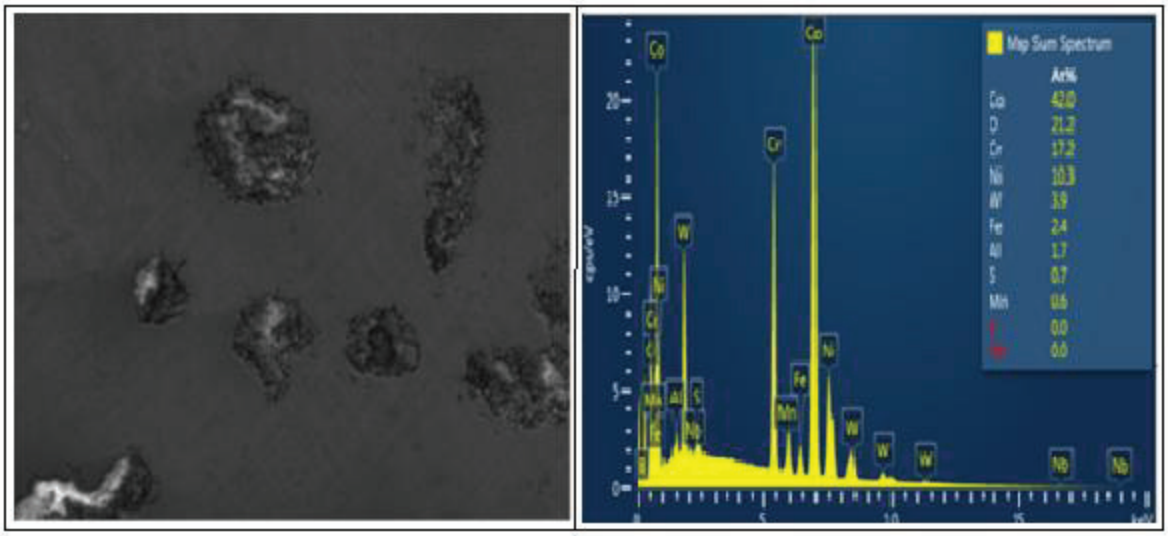

Figure 7. SEM–EDS microstructure of the transition zone of the sample abraded at 350 °C.

Figure 8 illustrates the friction coefficient–time curves obtained from reciprocating wear tests conducted at 350 °C on untreated Haynes 25 samples and those borided at 975 °C for 5 h and subsequently cooled in furnace, air, and water environments. The friction coefficient values were determined using ball-on-disk experiments under dry sliding conditions, and the data were plotted at a test temperature of 350 °C. Analysis of the curves shows that the untreated alloy has a lower friction coefficient than the borided specimens cooled under the various conditions. Although samples subjected to different cooling rates exhibit higher friction coefficients than the untreated alloy, borided samples exhibit an interesting trend: as the cooling rate increases from furnace to air to water, the friction coefficient tends to decrease and becomes more stable over time. The comparatively higher friction coefficients observed for the borided samples are linked to increased surface roughness caused by the boriding treatment. With a rougher surface, the Al_2O_3 counter ball penetrates the coating less, allowing easier sliding and reducing contact pressure (Gündoğar, 2024; Li et al., 1996). Consequently, the abrasive ball contacts a smaller effective area, and because the contact stresses are locally greater, it tends to slide more rapidly across the surface. Moreover, Figure 8 indicates that the untreated alloy exhibits friction behavior as that at room temperature, whereas the borided and cooled samples exhibit higher friction coefficients at elevated temperatures. This can be attributed to the open-air conditions of the 350 °C tests, where roughened surfaces undergo oxidation during cyclic loading. The oxides formed between the Al_2O_3 ball and the sample surface act as additional abrasives.

This interpretation is supported by oxygen detected on worn surfaces in later EDS analyses, and is consistent with previously reported findings (Kramer et al., 1998; Günen et al., 2017).

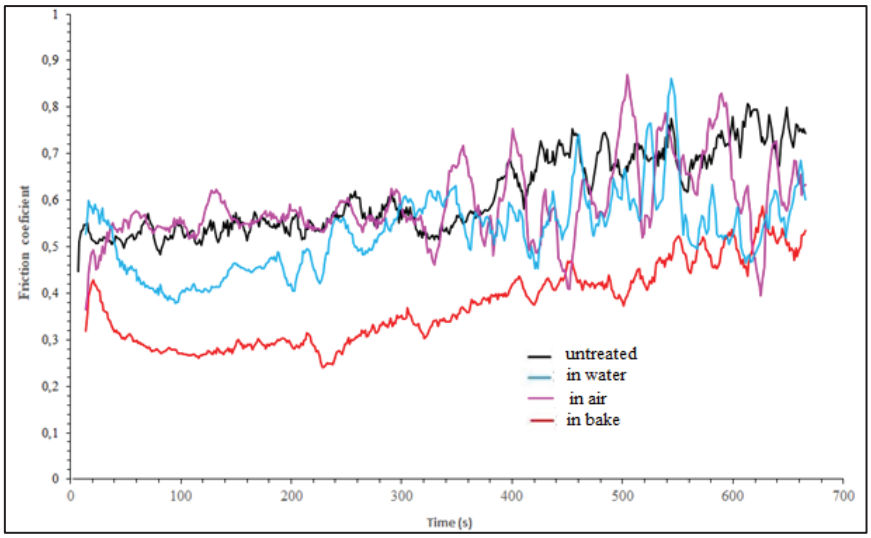

Figure 8. Friction coefficient–time graph of the Haynes 25 sample abraded at 350 °C.

During the wear experiments conducted at 350 °C, all specimens transitioned into a steady-state wear regime after a relatively short sliding distance. This behavior is evidenced by the friction coefficient curves, which level off after roughly 100 seconds. When the test temperature is raised to 350 °C, the borided samples show a slight increase in friction coefficient, whereas the untreated specimens show a reduction in friction. The friction coefficient is predominantly influenced by surface-related factors such as hardness, roughness, lubrication conditions, and localized chemical interactions at the interface of the contacting surfaces (Peng et al., 2018). The comparatively lower CoF values recorded for the substrate material at elevated temperatures may be attributed to oxidation. At high temperatures, the alloying elements in the substrate tend to oxidize more readily, thereby reducing friction. Numerous studies have reported that oxide films formed during sliding can provide lubrication, thereby lowering the friction coefficient (Günen et al., 2017; Günen, 2020). Conversely, a slight increase in CoF with increasing temperature has been observed in the borided samples. The condition of the worn surfaces can explain this: in the borided samples cooled in air and water, the rough surfaces oxidize due to the repeated loading, and this oxide layer becomes trapped between the ball and the substrate, making it more difficult for the ball to move on the worn surface, causing abrasive effects, and increasing the friction coefficient (Hawkins, 1998).

The untreated Haynes 25 sample, the borided samples, and the samples cooled in furnace, air, and water environments were subjected to wear tests at 350 °C, and their wear scar profiles were determined. A 2D contact profilometer was used for measuring the wear scar profiles of these samples. Figure 9 illustrates the wear track depths and corresponding measurement lengths captured

through profilometer analysis. Based on these profiles, the depths and widths of the wear scars were determined, allowing for the calculation of wear volume loss and wear rate. A concise summary of these calculated values is provided in Table 1. According to Table 1, the untreated Haynes 25 specimen exhibited the widest and deepest wear track during the 350 °C wear test. Conversely, the borided samples, regardless of whether they were cooled in water, air, or a furnace, displayed substantially smaller wear scar dimensions under the same test conditions. This confirms that the boride layer produced during boriding significantly enhances the Haynes 25 alloy's resistance to the penetrating action of the Al_2O_3 counterbody, thereby improving its wear performance. An examination of Table 1 and Figure 9 shows that, during wear at 350 °C, the untreated specimen possesses the greatest wear scar depth and width. Increasing the cooling rate reduces the scar depth from 3.4 mm to 2.7 mm, while the scar width increases slightly, from 996.67 mm to 1050 mm. Moreover, when the results of borided samples cooled under different media, water, air, and furnace, are compared at identical temperature and test duration, it becomes evident that the hardness improvements induced by faster cooling rates contribute positively to the alloy's wear resistance (see Figure 3). The reduced scar depths observed in the borided samples can be attributed to the boride layer's enhanced resistance to indentation and deformation by the Al_2O_3 ball, demonstrating superior wear resistance. Additionally, profilometer scans reveal that both borided and unborided specimens exhibit wider, deeper wear tracks at 350 °C than at room temperature, an expected outcome due to thermal softening at elevated temperatures.

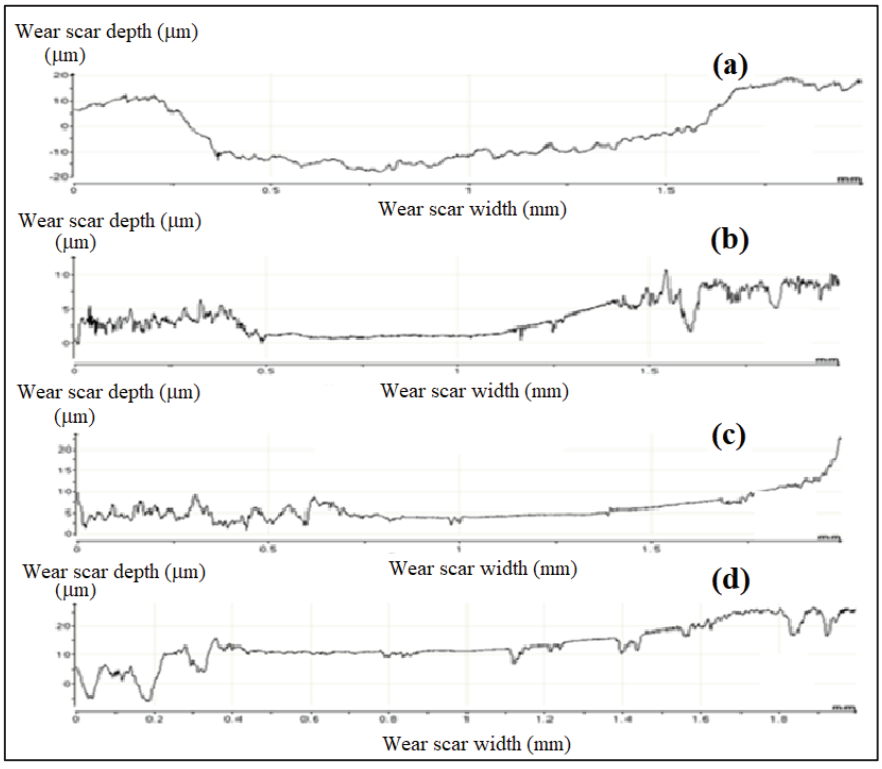

Figure 9. Profilometer scans of wear scar depths on the samples worn at 350 °C: (a) untreated, (b)

furnace-cooled, (c) air-cooled, and (d) water-quenched.

Table 1: Compilation of wear trace depth and width values obtained from the Haynes 25 specimens.

Wear test temperature	Samples	Wear scar depth (μm)	Wear scar width (μm)	Wear rate (mm^3/Nm)x10^{-5}
24°C	Untreated	13,0	1361,67	13,10
	İn bake	4,3	825	2,62
	İn air	4,2	788	2,49
	in water	3,77	750	2,09
350°C	Untreated	20,0	1400	20,72
	İn bake	3,4	996,67	2,53
	İn air	3,1	1095	2,54
	in water	2,7	1050	2,12

This outcome is expected, as thermal softening at elevated temperatures enables the abrasive ball to penetrate more deeply into the underlying material. The 2D profilometer traces presented in Figure 7 corroborate this observation. Moreover, when the wear scar depths and widths of untreated and borided samples at room temperature are compared, the data in Table 1 reveal that boriding yields a more substantial enhancement in wear resistance at ambient temperature than at elevated temperatures. Comparable trends have been documented in previous research (Liu et al., 2018; Gunen et al., 2022; Metals Handbook, 1983; Rai et al., 2021). Following wear testing at 350 °C, all borided specimens displayed smaller wear scar depths relative to the unborided sample (for instance, 20 μm vs. 25.6 μm). The boride layer thicknesses for the furnace-cooled, air-cooled, and water-quenched specimens were approximately 51.14 μm, 51.93 μm, and 52.6 μm, respectively. Although the coating layer thicknesses were nearly identical, the wear scar depths varied according to the wear test temperature (24 °C versus 350 °C). Notably, the water-quenched specimen exhibited the shallowest wear scar at 350 °C, indicating that water cooling after boriding increases substrate hardness (as evidenced in Table 1 and Figure 3), thereby improving wear resistance under elevated-temperature conditions.

Acknowledgement

This work was financially supported by the Karabük University Scientific Research Projects Coordination Unit under project code KBÜBAP-23-YL-008. The authors acknowledge the KBÜ-BAP unit for its support.

REFERENCES

- Ahmed, R., de Villiers Lovelock, H.L., & Davies, S. (2021). Sliding wear of blended cobalt-based alloys. *Wear*, 466, 203533.
- Campos-Silva, I., Bravo-Bárcenas, D., Cimenoglu, H., Figueroa-López, U., Flores-Jiménez, M., & Meydanoglu, O. (2014). The boriding process in CoCrMo alloy: Fracture toughness in cobalt boride coatings. *Surface & Coatings Technology*, 260, 362–368.
- Campos-Silva, I., Contla-Pacheco, A.D., Figueroa-López, U., Martínez-Trinidad, J., Garduño-Alva, A., & Ortega-Avilés, M. (2019). Sliding wear resistance of nickel boride layers on an Inconel 718 superalloy. *Surface & Coatings Technology*, 378, 124862.
- Campos-Silva, I., Rodriguez-Castro, G. (2015). Boriding to improve the mechanical properties and corrosion resistance of steel. In Mittemeijer, E. & Somers, A. (Eds.), *Thermochemical Surface Engineering of Steels*. Woodhead Publishing, pp. 651–702.
- Campos-Silva, I., Vega-Morón, R.C., Reséndiz-Calderón, C.D., Bravo-Bárcenas, D., Eryilmaz, O.L., Kahvecioglu-Feridun, O., & Rodríguez-Castro, G. (2019). Dry sliding wear resistance of cobalt boride coatings formed on ASTM F1537 alloy. *Journal of Materials Engineering and Performance*, 28(4), 2399–2410.
- Chen, L., Xu, T., Lu, S., Wang, Z., Chen, S., & Zhang, L. (2018). Improved hardness and wear resistance of plasma sprayed nanostructured NiCrBSi coating via short-time heat treatment. *Surface & Coatings Technology*, 350, 436–444.
- Costa, A.M.S., Oliveira, J.P., Escobar, J.D., Salvador, C.A.F., Monteiro, M.J., Poplawsky, J.D., & Tschiptschin, A.P. (2022). Secondary phase partitioning after solution and aging treatments in a Co–Ni superalloy. *Materials Letters*, 309, 131377.
- Coutsouradis, D., Davin, A., & Lamberigts, M. (1987). Cobalt-based superalloys for gas turbine applications. *Materials Science and Engineering*, 88, 11–19.
- Cuao-Moreu, C.A., Hernández-Sanchéz, E., Alvarez-Vera, M., Garcia-Sanchez, E.O., Perez-Unzueta, A., & Hernandez-Rodriguez, M.A.L. (2019). Tribological behavior of borided CoCrMo cast alloy. *Wear*, 426, 204–211.
- De Faria Cunha, F.A., de Andrade Reis, R., Gonçalves, S.P., Fernandes, F.A.P., Baldan, R., & de Sousa Malafaia, A.M. (2023). Cyclic oxidation of conventional and Nb-modified MAR-M246. *Coatings*, 13, 519.
- Deng, D.W., Wang, C.G., Liu, Q.Q., & Niu, T.T. (2015). Microstructure and properties of borided Inconel 718. *Transactions of Nonferrous Metals Society of China*, 25, 437–443.
- Doñu-Ruiz, M.A., López-Perrusquia, N., Renteria-Salcedo, A., Flores-Martinez, M., Rodriguez-De Anda, E., Muhl, S., & García, E. (2021). Tribocorrosion of borided CoCrMo in NaCl. *Surface & Coatings Technology*, 425, 127698.
- Du, Y., Chen, H., Yang, G., Liu, B., Gao, Y., & Luo, H. (2018). Cobalt content effects on TiC–Co tribology. *Ceramics International*, 44, 14186–14194.
- Gialanella, S., & Malandruccolo, A. (2020). Superalloys. In *Aerospace Alloys*. Springer, pp. 267–386.
- Girişken, İ., & Güral, Ç. (2023). Microstructure and high-temperature wear of pack-borided Haynes 25. *CIRP Journal of Manufacturing Science and Technology*, 45, 82–98.
- Gualanella — duplicate removed (already included).
- Gündoğar, A. (2024). *Kobalt esaslı Haynes 25 süper alaşımının aşınma ve korozyon davranışı*. MSc Thesis, Karabük University.
- Günen, A. (2020). High-temperature dry sliding wear of boronized Inconel 718. *Metallurgical and Materials Transactions A*, 51, 927–939.
- Günen, A., & Ergin, Ö. (2023). Characterization and high-temperature wear of thermochemical coatings on Haynes 25. *Coatings*, 13, 1272.
- Günen, A., Kanca, E., Çakır, H., Karakaş, M.S., Gök, M.S., & Küçük, Y. (2017). Borotitanizing of Inconel 625. *Surface & Coatings Technology*, 311, 374–382.

- Günen, A., Kanca, Y., Karahan, İ.H., Karakaş, M.S., Gök, M.S., Kanca, E., & Çürük, A. (2018). Coating techniques on STKM-13A corrosion. *Metallurgical and Materials Transactions A*, 49(11), 5833–5847.
- Gunes, I. (2013). Kinetics of borided gear steels. *Sadhana*, 38(3), 527–541.
- Gunes, I. (2022). Corrosion of construction steel in acidic media. *Journal of Characterization*, 2(2), 161–166.
- Hao, E., An, Y., Zhao, X., Zhou, H., & Chen, J. (2018). NiCoCrAlYTa coatings & wear resistance. *Applied Surface Science*, 462, 194–206.
- Hawkins, M.J. (1998). Recovering cobalt from primary and secondary sources. *JOM*, 50(10), 46–50.
- Keddam, M., & Chentouf, S.M. (2005). Diffusion model for FeB/Fe2B bilayers. *Applied Surface Science*, 252, 393–399.
- Kramer, D.P., McDougal, J.R., Ruhkamp, J.D., et al. (1998). Haynes 25 alloy for power systems. *AIP Conference Proceedings*, 420, 1167–1172.
- Kulka, M. (2019). *Current Trends in Boriding Techniques*. Springer.
- Li, J.B., Xu, H.B., Chen, R., & Wang, Z.G. (1996). Plastic deformation and half-width. *Metallurgical and Materials Transactions A*, 27A, 3662–3668.
- Liu, L., Xiao, J., Wei, X., Ren, Y., Zhang, G., & Zhang, C. (2018). Plasma sprayed FeCrBSi coatings: temperature & atmosphere effects. *Journal of Alloys and Compounds*, 753, 586–594.
- Mapelli, C., Casalino, C., Strada, A., et al. (2020). Oxidation–sulphidation of Ni & Co alloys. *Journal of Materials Research and Technology*, 9, 15679–15692.
- Metals Handbook. (1983). Ninth Edition, Vol. 10. ASM International.
- Motallebzadeh, A., Atar, E., & Cimenoglu, H. (2015). Sliding wear of Stellite 12. *Tribology International*, 91, 40–47.
- Mu, D., & Shen, B.L. (2010). Oxidation resistance of boronized CoCrMo. *International Journal of Refractory Metals and Hard Materials*, 28, 424–428.
- Mu, D., Shen, B.-L., & Zhao, X. (2010). Boronizing effects on CoCrMo mechanical and wear. *Materials & Design*, 31(8), 3933–3936.
- Öge, M., Küçük, Y., Öğe, T.Ö., Günen, A., & Kanca, Y. (2023). Boriding effects on CoCrMo tribology. *Tribology International*, 187, 108697.
- Peng, F., Ruiqing, C., Zhijun, X., Guanjun, D., & Chuanhai, J. (2018). Hardness vs FWHM after peening. *Applied Surface Science*, 431, 165–169.
- Rai, A.K., Paul, C.P., Mishra, G.K., Singh, R., & Bindra, K.S. (2021). Laser boriding of Inconel 718. *Journal of Materials Processing Technology*, 298, 117298.
- Safavi, M.S., & Rasooli, A. (2019). Ni-P-TiO2 nanocomposites. *Surface & Coatings Technology*, 372, 252–259.
- Sato, J., Omori, T., Oikawa, K., Ohnuma, I., Kainuma, R., & Ishida, K. (2006). Cobalt base high-temperature alloys. *Science*, 312, 90–91.
- Vashishtha, N., Sapate, S.G., Bagde, P., & Rathod, A.B. (2018). Heat treatment and wear of WC–12Co and Cr_3C_2–25NiCr. *Tribology International*, 118, 381–399.
- Wang, H., He, P., Ma, G., Xu, B., Xing, Z., & Chen, S. (2018). CNT-reinforced TiO_2 coatings. *Journal of the European Ceramic Society*, 38, 3660–3672.
- Wang, S.Y., Sun, Y., Hou, X.Y., Cui, C.Y., Sun, X.F., & Zhou, Y.Z. (2020). Brazed joint of Co-based superalloy. *Vacuum*, 177, 109413.
- Wang, Y., Liu, J., Kang, N., Darut, G., Poirier, T., & Stella, J. (2016). Cavitation erosion of CoMoCrSi. *Tribology International*, 102, 429–435.
- Yang, W., Zou, L., Cao, X., Liu, J., Li, D., & Cai, Z. (2019). HVOF-sprayed CoMoCrSi coatings. *Surface & Coatings Technology*, 358, 994–1005.